

## Influence of relativistic contributions to the effective potential on the electronic structure of Pd and Pt

A. H. MacDonald

*National Research Council, Ottawa K1A 0R6, Canada*

J. M. Daams\* and S. H. Vosko

*University of Toronto, Toronto M5S 1A7, Canada*

D. D. Koelling

*Argonne National Laboratory, Argonne, Illinois 60439*

(Received 22 December 1980)

The influence of relativistic-interaction corrections to the energy density functional in the density functional formalism is examined using explicit calculations for Pd and Pt. We present and compare three separate self-consistent density-functional calculations which included (1) exchange only, (2) exchange and correlation, and (3) exchange and correlation plus relativistic-interaction corrections. Since they are of comparable or larger size, we have included and examined the effects of relativistic kinematics and non-muffin-tin potential shapes. Because the relativistic interaction corrections are significant only very near the nucleus, we report separately results for the core levels and for the valence states. The corrections obtained were negligible for Pd and small but significant for Pt.

### I. INTRODUCTION

In this paper we report on self-consistent band-structure calculations for palladium and platinum. Pd and Pt are, respectively, 4*d* and 5*d* transition metals with nearly filled *d* bands. They are of interest because of their large paramagnetic susceptibilities and associated magnetic properties, their interesting alloying properties, and their importance in catalysis. As a result, they have received a great deal of attention and there is a wealth of experimental data on well-characterized samples of exceptional quality. Similarly, there have been many theoretical calculations on these two materials and numerous hypotheses proposed concerning them.<sup>1</sup> We have examined only a subset of these properties, namely those directly related to the band structure, more or less rigorously within the framework of density functional theory.<sup>2</sup> A major objective of this study was to examine the result of including the relativistic contributions to the interparticle forces in the theory and to compare their effects to the correlation effects. (This is, of course, in addition to the standard inclusion of relativistic kinematics.)

Density functional theory is a remarkable tool within many-body theory. By solving a set of single-particle equations for auxiliary particles self-consistently, one is able to determine the distribution of electrons in the metal, i.e., the electron charge and spin density, as well as the total energy of the metal and quantities related to the energy such as the magnetic susceptibility, equilibrium lattice constant, and bulk modulus.<sup>3</sup> For the properties mentioned above, the only quantity

which needs to be approximated is the exchange-correlation (xc) energy functional  $E_{xc}[n]$  which appears in the formalism, and there is a good deal of evidence that even the simplest approximation for  $E_{xc}[n]$ , the local density approximation (LDA), is adequate in most cases.<sup>3</sup> Of equal importance, however, is the effective-independent-particle model of the metal provided by the energies and wave functions which are the solutions of the single-particle equations. This model is, in fact, the basis of much of our understanding of the properties of individual metals. While this model is on less firm theoretical footing, it provides, in most cases, the best available description of the ground state and excited states of transition metals. Moreover, noting the sensitivity of electronic properties to details of the band structure, we believe that any more sophisticated description of these metals must be built around and contain the very substantial physical content of this level of description.

The relativistic effects on the interaction forces are relatively minor corrections compared to the relativistic kinematic corrections, but inserted directly they pose serious problems to the self-consistency process. Thus it is appealing to include them in the same manner as the exchange-correlation effects by including their contribution to the energy functional in a local approximation. This extension of density functional theory, described previously<sup>4</sup> and briefly reviewed in Sec. II, can be expected to facilitate the study of the systems at the upper end of the Periodic Table. Here we examine the effect of these relativistic corrections. In order to do so, we have per-

formed calculations which avoid many of the approximations commonly used since these could influence our results. The methods used are outlined in Sec. III to establish the level of precision maintained. In Sec. IV, the resulting crystal potentials, electron densities, single-particle energies, and magnetic susceptibilities are presented, each of these quantities having been calculated using several different approximations to the xc potential with the aim of examining their sensitivity in this respect. Finally, Sec. V contains some concluding remarks.

## II. RELATIVISTIC SINGLE-PARTICLE EQUATIONS

The equations which we wish to solve are the relativistic generalizations<sup>4</sup> of the Kohn-Sham single-particle equations<sup>5</sup>:

$$(-i\hbar c \alpha \vec{p} + \beta m c^2 + V_{\text{eff}}[n; \vec{r}])\psi_i(\vec{r}) = \epsilon_i \psi_i(\vec{r}), \quad (1a)$$

$$n(\vec{r}) = \sum_i \psi_i^\dagger(\vec{r})\psi_i(\vec{r})\Theta(\mu - \epsilon_i), \quad (1b)$$

$$Q = -e \sum_i \Theta(\mu - \epsilon_i), \quad (1c)$$

$$V_{\text{eff}}[n; \vec{r}] = V(\vec{r}) + V_H[n; \vec{r}] + V_{\text{xc}}[n; \vec{r}], \quad (1d)$$

where  $Q$  is the total electronic charge of the met-

al,  $V(\vec{r})$  is the potential from the atomic nuclei,  $V_H[n; \vec{r}]$  is the classical electrostatic potential,  $V_{\text{xc}}[n; \vec{r}]$  is the xc potential (discussed below), and the sums over  $i$  are over positive energy states only (our notation is standard<sup>6</sup>). Note that these equations must be solved self-consistently since the effective potential is a functional of the electron density which is in turn expressed in terms of the eigenspinors of the Dirac-type single-particle equations. The LDA for  $V_{\text{xc}}[n; \vec{r}]$  (Ref. 4) may be expressed in units of Ry in the form

$$V_{\text{xc}}^{\text{LDA}}[n; r] = \left(\frac{81n(\vec{r})}{4\pi}\right)^{1/3} \alpha(n(\vec{r})), \quad (2)$$

where  $n(\vec{r})$  is in atomic units and the dimensionless function  $\alpha(n)$  is dependent on the approximation for the uniform electron gas energy. In the non-relativistic case correlations increase  $\alpha$  from the Hartree-Fock (HF) value,  $\alpha(n) = \frac{2}{3}$  which is correct in the high-density limit, to  $\alpha \sim 0.9$  at the lowest occurring metallic densities.<sup>7</sup> In the relativistic case, corrections occur at very high densities corresponding to current-current interactions and other quantum electrodynamical contributions to the energy so that the high-density limit becomes  $\lim_{n \rightarrow \infty} \alpha(n) = -\frac{1}{3}$ . The variations of  $\alpha$  with  $n$  are illustrated in Fig. 1.

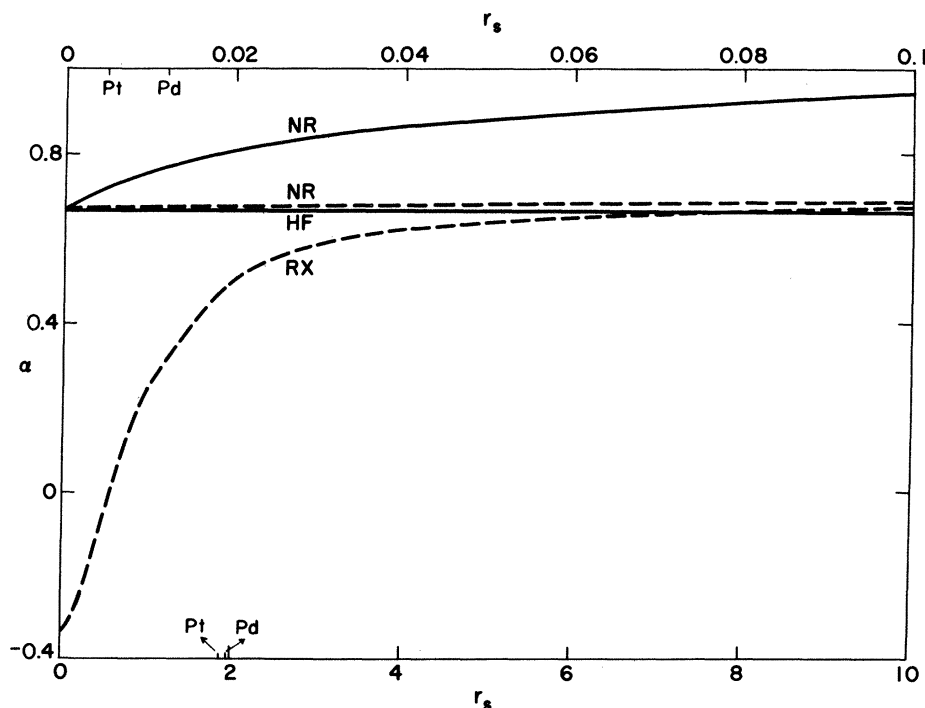


FIG. 1. Exchange-correlation potentials expressed in terms of the parameter  $\alpha$  [Eq. (2)] as a function of density in terms of the parameter  $r_s = (\frac{3}{4}\pi n a_0^3)^{1/3}$ . The curves are labeled as in Eq. (3). The solid curves refer to the lower axis  $r_s$  scale and the dashed curves refer to the upper  $r_s$  scale which expands the high-density region. Minimum (upper scale) and maximum (lower scale)  $r_s$  values for Pd and Pt are indicated.

In this work we have performed calculations using three separate approximations for the xc potential:

$$\alpha^{\text{HF}}(n) \equiv \frac{2}{3}, \quad (3a)$$

$$\alpha^{\text{NR}}(n) = \frac{2}{3} [1 + 0.0545 r_s \ln(1 + 11.4/r_s)], \quad (3b)$$

$$\alpha^{\text{RX}}(n) = \frac{2}{3} \left\{ 1 - \frac{3}{2} [(\beta\eta - \ln\delta)/\beta^2]^2 + 0.0545 r_s \ln(1 + 11.4/r_s) \right\}, \quad (3c)$$

where  $r_s = (\frac{3}{4}\pi n a_0^3)^{1/3}$  is the usual conduction-electron density parameter,  $\beta = \chi_c k_F(n) = (9\pi/4)^{1/3} \alpha/r_s$ ,  $\alpha = 1/137$  is the fine-structure constant (and will not be used further to avoid confusion),  $\eta = (1 + \beta^2)^{1/2}$ , and  $\delta = \beta + \eta$ .  $\alpha^{\text{NR}}$  incorporates correlation corrections to  $\alpha^{\text{HF}}(n)$  in the approximation of Gunnarsson *et al.*<sup>8</sup> while  $\alpha^{\text{RX}}(n)$  includes, in addition, relativistic corrections to the exchange part of the energy.<sup>4</sup> By comparing results from  $\alpha^{\text{NR}}(n)$  and  $\alpha^{\text{HF}}(n)$  we can identify the role played by correlation corrections within this scheme. Similarly, comparing results from  $\alpha^{\text{NR}}(n)$  and  $\alpha^{\text{RX}}(n)$  will reveal the influence of the intrinsically relativistic contribution to the xc potential.

### III. METHOD OF CALCULATION

For a given crystal potential Eq. (1a) was solved using a relativistic generalization of the linearized augmented plane-wave (APW) method.<sup>9,10</sup> The method, which is described in more detail elsewhere,<sup>11</sup> allows spin-orbit interactions to be separated and treated more efficiently than in the standard relativistic APW method. We will refer to the above as a spin-orbit-linearized augmented plane-wave (SO-LAPW) method. In the course of iterating Eqs. (1) to self-consistency the spin-orbit interactions were not included in solving Eq. (1a). This point is discussed later. The charge density is constructed from eigenspinors in a manner similar to that discussed by Elyashar and Koelling.<sup>12</sup> For the valence states the sum over "i" of Eq. (1b) becomes a sum over bands and an integral over the Brillouin zone (BZ). This integral can be reduced to the irreducible region (IR) of the BZ by summing only the cubic symmetric components. To evaluate the integral, we have used a mesh derived from the centers of tetrahedra with roughly a  $\pi/8a$  edge size which yields 128 distinct points in the IR. To test convergence, calculations have also been performed using another mesh with 24 points in the IR.

The charge density is obtained as a Kubie harmonic expansion inside the muffin-tin spheres,  $4\pi r^2 n(\vec{r}) = [\sigma_0(r) + \sigma_4(\hat{r})K_4(\hat{r}) + \sigma_6(r)K_6(\hat{r}) + \dots]$  (4a) and a plane-wave expansion in the interstitial region

$$n(\vec{r}) = \sum_m n_m \sum_j \exp(i\vec{G}_j^m \cdot \vec{r}). \quad (4b)$$

In Eq. (4a),  $r$  is the distance from the center of the muffin-tin sphere while  $K_4(\hat{r})$  and  $K_6(\hat{r})$  are the leading order Kubie harmonics,

$$K_4(\hat{r}) = \left(\frac{7}{12}\right)^{1/2} Y_{4,0}(\hat{r}) + \left(\frac{5}{24}\right)^{1/2} [Y_{4,4}(\hat{r}) + Y_{4,-4}(\hat{r})] \quad (5a)$$

$$K_6(\hat{r}) = \left(\frac{2}{6}\right)^{1/2} Y_{6,0}(\hat{r}) - \left(\frac{7}{4}\right)^{1/2} [Y_{6,4}(\hat{r}) + Y_{6,-4}(\hat{r})]. \quad (5b)$$

The convergence of this expansion is discussed later. In Eq. (4b)  $\vec{G}_j^m$  is the  $j$ th member of the  $m$ th star of reciprocal-lattice vectors. A similar representation has been used for  $V_{\text{eff}}[n; \vec{r}]$ ; the techniques used to construct the potential in this dual representation from the corresponding representation for the charge density have been discussed previously.<sup>13</sup>

In iterating to self-consistency, input and output charge densities for one iteration were mixed to form the input charge densities for the next iteration. Self-consistency was considered to have been achieved when no energy on the IR integration mesh changed by more than 0.2 mRy, the maximum relative change in  $\sigma_0(r)$  was less than 0.1%, and the maximum relative changes in  $\sigma_4(r)$  and  $\sigma_6(r)$  were less than 0.2%. With reasonable starting densities, e.g., overlapping atomic, and judicious choices for the charge-density mixing parameter at each step,<sup>12</sup> ~20 iterations were required to reach self-consistency.

Once a self-consistent effective potential has been found, a number of properties can be expressed in terms of the solutions of Eq. (1a). In the following paragraphs we mention those properties which we have calculated and discuss the techniques used for their evaluation. The physical significance of these properties and of our results will be discussed in more detail in Sec. IV.

Several derivative properties can be expressed as integrals over the BZ of combinations of the eigenvalues and eigenspinors of Eq. (1a):

$$N(\epsilon) = 2 \sum_{n, \vec{k}} \theta(\mu - \epsilon_{n, \vec{k}}), \quad (6)$$

$$D(\epsilon) = N'(\epsilon) = 2 \sum_{n, \vec{k}} \delta(\epsilon - \epsilon_{n, \vec{k}}), \quad (7)$$

$$\langle g^2(\epsilon) \rangle = 8 \left( \sum_{n, \vec{k}, \lambda} \left| \int^{dr} \psi_{n, \vec{k}, \lambda}^\dagger(\vec{r}) \beta \sigma_z \psi_{n, \vec{k}, \lambda}(\vec{r}) \right|^2 \right) \times \epsilon(\epsilon - \epsilon_{n, \vec{k}}) / D(\epsilon), \quad (8)$$

$$\langle V^2(\epsilon) \rangle = 2 \left( \sum_{n, \vec{k}} \delta(\epsilon - \epsilon_{n, \vec{k}}) (\nabla_{\vec{k}} \epsilon_{n, \vec{k}} \cdot \nabla_{\vec{k}} \epsilon_{n, \vec{k}}) \right) / D(\epsilon), \quad (9)$$

$$\gamma(\vec{r}) = 2 \left( \sum_{n, \vec{k}} \delta(\mu - \epsilon_{n, \vec{k}}) \psi_{n, \vec{k}}^\dagger(\vec{r}) \psi_{n, \vec{k}}(\vec{r}) \right) / D(\epsilon). \quad (10)$$

$N(\epsilon)$  and  $D(\epsilon)$  are, respectively, the number of states below energy  $\epsilon$  and the density of states at energy  $\epsilon$ .  $\langle V^2(\epsilon) \rangle$  is the average of the square of the electron group velocity over the surface of constant energy  $\epsilon$  and is a useful quantity in transport theory.  $\langle g^2(\epsilon) \rangle$  is the square of an effective  $g$  factor averaged over the surface of constant energy  $\epsilon$ . This spin-only  $g$  factor<sup>14</sup> reflects the splitting of the time-reversed degenerate states distinguished by the index  $\lambda$  in Eq. (8) in a magnetic field which couples only to their spin magnetic moment. The reduction of this  $g$  factor from 2 may be interpreted as representing the inability of the electrons to line their moments up with the field because of the partial mixing of spins in the spinors.  $\gamma(\vec{r})$  gives the shape of the charge density from the electrons at the Fermi surface and is expected<sup>15</sup> to be nearly proportional to the magnetization induced in these metals by an applied magnetic field. All of these quantities have been evaluated using the tetrahedron method.<sup>16,17</sup> Single-particle eigenvalues and spin-only  $g$  factors were determined at 933 distinct  $\vec{k}$  points at the vertices of 4096 tetrahedra in the IR. Using the hybrid tetrahedron method,<sup>18</sup>  $N(\epsilon)$ ,  $D(\epsilon)$ ,  $\langle V^2(\epsilon) \rangle$ , and  $\langle g^2(\epsilon) \rangle$  and  $\gamma(\vec{r})$  then evaluated using 32 768 tetrahedra. In evaluating  $\langle V^2(\epsilon) \rangle$  the usual tetrahedron method assumption of constant  $\nabla_{\vec{k}} \epsilon_{n, \vec{k}}$  was adopted. On the other hand, the variation of spin-only  $g$  factor across a tetrahedron was included for  $\langle g^2(\epsilon) \rangle$  and  $\gamma(\vec{r})$  using methods described elsewhere.<sup>18,19</sup> Note that in contrast to the other four quantities  $\gamma(\vec{r})$  is determined solely in terms of the eigenspinors at the Fermi surface.

The Fermi-surface properties most directly accessible to experiment are the extremal orbits and the cyclotron masses for these orbits. We have calculated these quantities using a direct orbit tracing technique similar to that discussed by Shaw *et al.*<sup>20</sup> The approaches differ in that here the derivative of the Fermi radius with respect to azimuthal angle, which is known in terms of the electron velocity, is used to improve the efficiency of the numerical integration. The electron velocities,  $\vec{V}_{n, \vec{k}} = \nabla_{\vec{k}} \epsilon_{n, \vec{k}}$ , were calculated using a Hellman-Feynman technique.<sup>21</sup> It should be noted that in obtaining extremal areas and cyclotron masses the electron energies were calculated using the full relativistic APW method to calculate eigenval-

ues, but using the self-consistent potentials obtained as described above. This point is discussed further in Sec. IV.

The Fourier components of the magnetization induced in a metal by a magnetic field can be measured by neutron scattering. For Pd, Pt the magnetic response is dominated by the spin component; in this case  $\gamma(\vec{r})$  should be nearly proportional to the induced magnetization.<sup>22,23</sup> After integrating over the Fermi surface  $\gamma(\vec{r})$  is expressed in the same form as  $n(\vec{r})$ :

$$4\pi r^2 N \gamma(\vec{r}) = [\gamma_0(r) + \gamma_4(r) K_4(\hat{r}) + \gamma_6(r) K_6(\hat{r})] \quad r \leq R \quad (11a)$$

$$N \gamma(\vec{r}) = \sum_m \gamma_m \sum_j \exp(i \vec{G}_j^m \cdot \vec{r}) \quad r \geq R. \quad (11b)$$

$N$  is the number of atoms in the metal. It follows that

$$\begin{aligned} \gamma(\vec{G}) &= \int d\vec{r} \exp(-i \vec{G} \cdot \vec{r}) \gamma(\vec{r}) \\ &= \int_0^{R_{dr}} \gamma_0(r) j_0(Gr) + K_4(\hat{G}) \int_0^{R_{dr}} \gamma_4(r) j_4(Gr) \\ &\quad - K_6(\hat{G}) \int_0^{R_{dr}} \gamma_6(r) j_6(Gr) \\ &\quad + \Omega_0 \sum_m \gamma_m \sum_j U(|\vec{G}_j^m - \vec{G}|). \end{aligned} \quad (12)$$

$U(G)$  is the Fourier transform of the step function which is zero inside the muffin-tin spheres:

$$U(G) = \left( \delta_{\vec{G}, \vec{0}} - \frac{4\pi R^2 j_1(GR)}{G} \right). \quad (13)$$

$\Omega_0$  is the unit-cell volume and  $j_1$  is a spherical Bessel function.

Another quantity of interest is the spin susceptibility  $\chi_p$ , which can be expressed in terms of  $D(\mu)$ ,  $\gamma(\vec{r})$ , and  $n(r)$  by<sup>22,23</sup>

$$\chi_p = 2.3768 D(\mu) [1 - D(\mu) I]^{-1} \quad (14a)$$

expressed in units of  $10^{-6}$  emu/mole

$$I = \left( \frac{9\pi}{8} \right)^{1/3} \int_{\Omega_0}^{d\vec{r}} \frac{[N_\gamma(\vec{r})]^2}{[n(\vec{r})]^{1/3}} J(n(\vec{r})), \quad (14b)$$

where  $I$  is in units of Ry,  $D(\mu)$  is in electrons per Ry atom, and  $n(\vec{r})$  is in atomic units.  $J(n) = \chi_0(n) / \chi_h(n) - 1$ , where  $\chi_0(n)$  and  $\chi_h(n)$  are the susceptibilities of the homogeneous noninteracting and homogeneous interacting electron gases, respectively. We have taken  $J(n)$  from the electron-gas calculation of Keiser and Wu,<sup>24</sup> as parametrized by Wilk *et al.*<sup>25</sup>  $I$  is the density-functional analog of the Stoner parameter. The significance of  $\chi_p$  when relativistic effects are important has been discussed previously<sup>15</sup> (see also Sec. IV). In evaluat-

ing  $I$ , we note that the integrand of Eq. (14b) is strongly dependent on  $\gamma(\vec{r})$  but is not particularly sensitive to  $n(\vec{r})$  [the integrand varies roughly as  $n(\vec{r})^{-2/3}\gamma(\vec{r})^2$ ]. We therefore feel justified in adopt-

ing the muffin-tin approximation for  $n(\vec{r})$  [but not  $\gamma(\vec{r})$ ] in this expression. This results in a much simpler calculational form:

$$I = \left(\frac{9\pi}{8}\right)^{1/3} \left[ \int_0^R dr J \left( \frac{\sigma_0(r)}{4\pi r^2} \right) \frac{\gamma_0^2(r)}{4\pi r^2} + \left( \gamma_4^2(r) + \frac{\gamma_6^2(r)}{(4\pi r)^2} \right) \left( \frac{\sigma_0(r)}{4\pi r^2} \right)^{1/3} + \frac{J(n_0)}{n_0^{1/3}} \sum_m \gamma_m \sum_{m'} \gamma_{m'} \sum_{j,j'} U(|G_j^m + G_{j'}^{m'}|) \right]. \quad (15)$$

#### IV. RESULTS AND DISCUSSION

##### A. Charge densities

Table I indicates how some representative features of the self-consistent charge densities depend on the IR integration mesh and the xc potential. First of all, we note that in going from the 24-point IR integration mesh to the 128-point mesh the change in  $n(\vec{r})$  is at most  $\sim 1\%$  at any point, with a tendency for the largest changes to occur in the non-muffin-tin parts of  $n(\vec{r})$ . This is consistent with the greater sensitivity of the non-muffin-tin components observed previously,<sup>26</sup> especially in light of the fact that the 24-point mesh was not quite uniform in sampling the Brillouin zone. As a result we consider the 128-point results to be well converged. Changes in other properties are similarly small.

Comparing HF and NR xc potential results we see that including correlation increases the density inside the muffin-tin sphere. The correlation contribution to the xc potential is attractive and larger in magnitude in the higher-density core region and, as a result, both lowers and narrows the  $d$  bands relative to the  $sp$  bands. (This is like increasing  $\alpha$  in an  $X\alpha$  calculation.) Both the increased localization of the  $d$ -wave functions and the increased occupancy of the atomiclike  $d$ -band states contribute to the decrease in interstitial charge. The relativistic corrections to the xc

potential make a repulsive contribution, the magnitude of which drops much more rapidly than the correlation contribution with increasing  $r_s$  (decreasing density) (see Fig. 1). The relativistic corrections have their largest influence on  $n(\vec{r})$  near the nuclear sites where they produce a decrease of  $\sim 1\%$ .

Figures 2 and 3 show the self-consistent  $\sigma_0(r)$ ,  $\sigma_4(r)$ , and  $\sigma_6(r)$  for Pd and Pt, respectively. For both Pd and Pt inside a radius of  $\sim 1.5$  a.u. the contribution to  $\sigma_4(r)$  comes from the incomplete filling of the  $d$  band; in each case the local maxima of  $\sigma_4(r)$  correlate with the peaks of the corresponding  $d$  radial wave function. Since similar contributions to  $\sigma_6(r)$  would require the presence of  $f$ -like states,  $\sigma_6(r)$  is essentially zero inside this radius. As the muffin-tin radius ( $R = 2.555$  a.u. for both Pd and Pt) is approached, the contributions to  $\sigma_4(r)$  and  $\sigma_6(r)$  increasingly reflect the re-expansion about one lattice site of the  $d$ -wave-function tails from neighboring lattice sites. We note that higher  $l$  components in the Kubic harmonic expansion of  $\sigma(\vec{r})$  would be essentially zero over even larger volumes and hence would have little impact on calculated energies. The main difference between the  $\sigma_4(r)$  and  $\sigma_6(r)$  obtained in a self-consistent calculation and the  $\sigma_4(r)$  and  $\sigma_6(r)$  obtained by overlapping atomic charge densities is the absence, in the latter case, of any contribution from the non-spherical character of the incomplete  $d$  band.

TABLE I. Features of self-consistent charge densities. All quantities are given in atomic units. The column labeled xc indicates the xc potential [Eq. (3)] and the number of points in the IR integration mesh.  $\sigma_0(R)$ ,  $\sigma_4(R)$ , and  $\sigma_6(R)$  give the charge density on the muffin-tin sphere and are indicative of the charge density in the interstitial region.  $n(0)$  is the charge density at the nucleus.  $a$  is the lattice constant used in this calculation.  $Q_0$  is the number of interstitial electrons.

Metal	xc	$a$	$\sigma_0(R)$	$Q_0$	$\sigma_4(R)$	$\sigma_6(R)$	$n(0)$
Pd	HF-128	7.340	3.202	0.9318	-0.664	-0.747	$1.294 \times 10^5$
Pd	NR-128	7.340	3.162	0.9007	-0.660	-0.744	$1.277 \times 10^5$
Pd	NR-24	7.340	3.161	0.9131	-0.667	-0.732	$1.279 \times 10^5$
Pd	RX-128	7.340	3.159	0.9066	-0.658	-0.742	$1.267 \times 10^5$
Pt	HF-128	7.398	4.016	1.295	-0.844	-1.004	$1.981 \times 10^6$
Pt	NR-128	7.398	3.959	1.210	-0.831	-0.997	$1.954 \times 10^6$
Pt	NR-24	7.398	3.969	1.229	-0.825	-0.995	$1.954 \times 10^6$
Pt	RX-128	7.398	3.956	1.209	-0.828	-0.993	$1.931 \times 10^6$

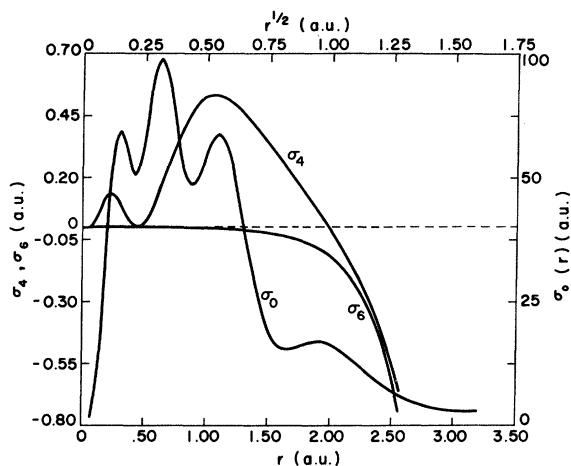


FIG. 2. Self-consistent charge density for Pd. The upper scale and right-hand scale refer to the  $\sigma_0(r)$  curve while the lower and left-hand scales refer to the  $\sigma_4(r)$  and  $\sigma_6(r)$  curves. Self-consistent densities from different xc potentials are indistinguishable on these scales.

This difference is even more dramatic for metals near the middle of a transition series.<sup>12</sup>

### B. Crystal potentials

The self-consistent crystal potentials obtained are illustrated for Pd and Pt in Figs. 4 and 5, respectively. The size of the non-muffin-tin terms is seen to be roughly the same in the two metals. Like  $\sigma_4(r)$  and  $\sigma_6(r)$ ,  $V_4(r)$  and  $V_6(r)$  become rapidly larger as  $r$  approaches the muffin-tin radius. This indicates that most of the non-muffin-tin character in the potentials comes from the tails of potentials associated with neighboring sites

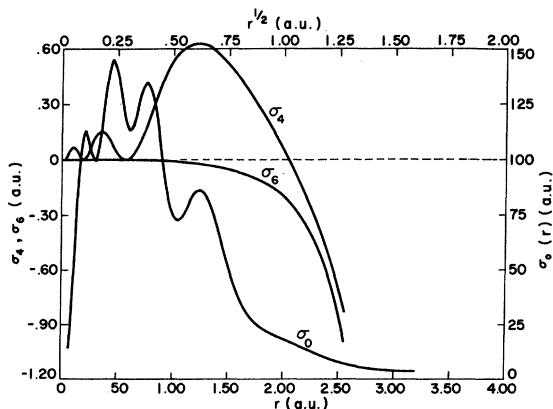


FIG. 3. Self-consistent charge density for Pt. The upper scale and right-hand scale refer to the  $\sigma_0(r)$  curve while the lower and left-hand scales refer to the  $\sigma_4(r)$  and  $\sigma_6(r)$  curves. Self-consistent densities from different xc potentials are indistinguishable on these scales.

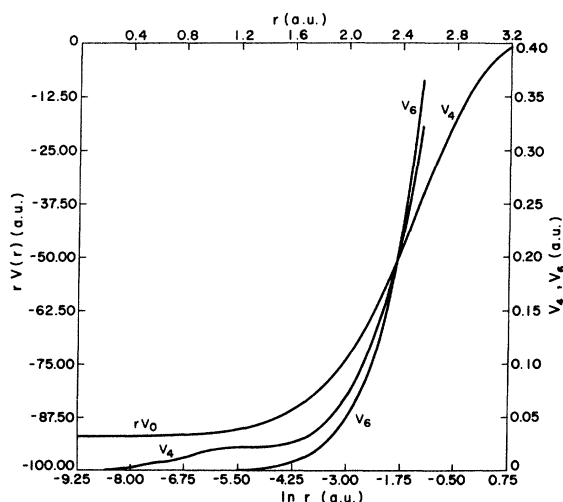


FIG. 4. Self-consistent crystal potential for Pd. The lower scale and left-hand scale refer to the  $rV_0(r)$  curve while the upper and right-hand scales refer to the  $V_4(r)$  and  $V_6(r)$  curves. Self-consistent potentials corresponding to different xc approximations are indistinguishable on these scales.

rather than from the asphericity of the potential associated with a given lattice site.

Comparing Figs. 4 and 5 with Figs. 2 and 3 we see that the Kubic harmonic expansion for the potential is not as rapidly convergent as the Kubic harmonic expansion of the charge density. In fact, while the charge density varies by 40% over the

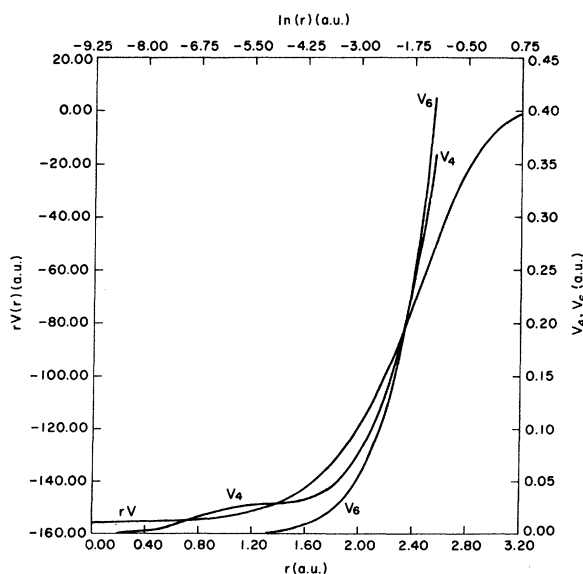


FIG. 5. Self-consistent crystal potential for Pt. The lower scale and left-hand scale refer to the  $rV_0(r)$  curve while the upper and right-hand scales refer to the  $V_4(r)$  and  $V_6(r)$  curves. Self-consistent potentials corresponding to different xc approximations are indistinguishable on these scales.

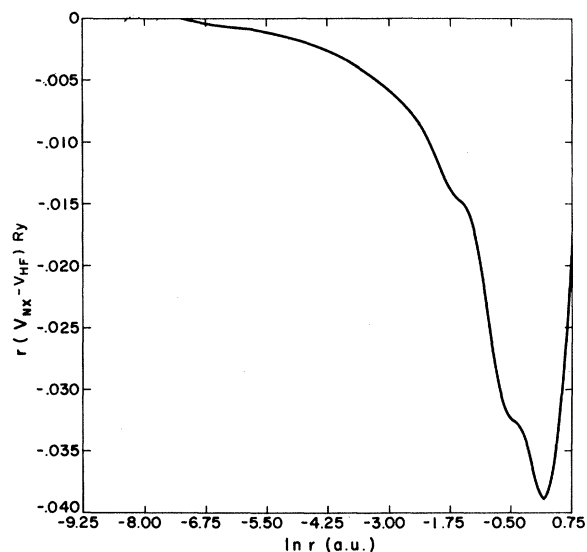


FIG. 6. Influence of correlation on the self-consistent crystal potential of Pd.

muffin-tin sphere surface, the crystal potential varies by  $\sim 0.2$  Ry, an energy comparable to the  $d$ -band width. Nevertheless, as we shall see, non-muffin-tin terms do not produce large changes in single-particle energies. The reason for this may be traced to the fact that the 5  $d$ -wave angular wave functions are well mixed in most metal wave functions so that most of the above-mentioned anisotropy in the potential is nearly averaged out state by state.

The influence of correlation on the crystal potential is shown in Figs. 6 and 7 for Pd and Pt, respectively, by plotting  $r [V_0^{\text{NR}}(r) - V_0^{\text{HF}}(r)]$  inside

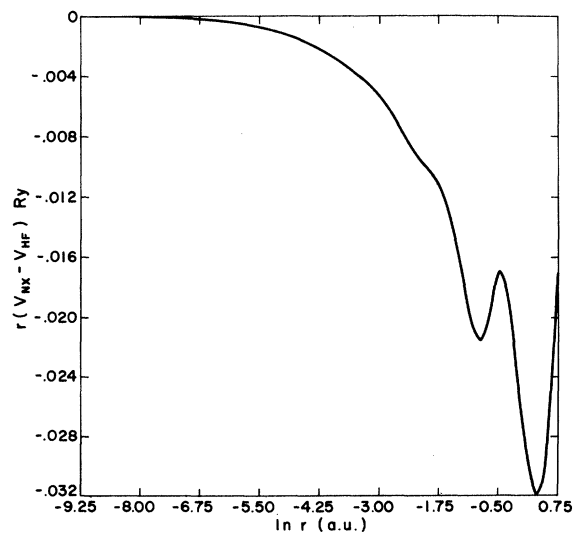


FIG. 7. Influence of correlation on the self-consistent crystal potential of Pt.

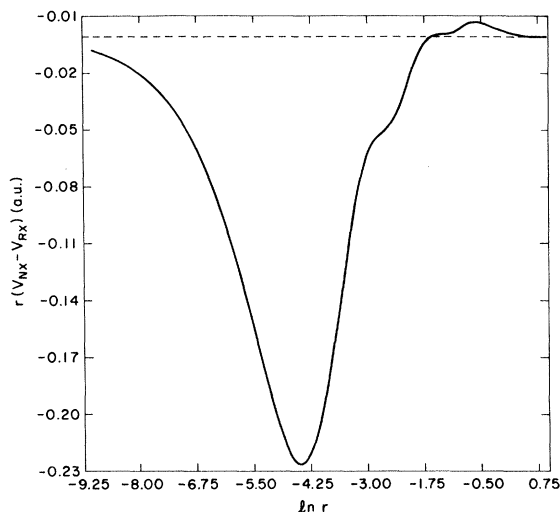


FIG. 8. Influence of the relativistic exchange correction on the self-consistent crystal potential of Pd.

the muffin-tin sphere. In studying these figures it should be noted that for each potential, energies are measured relative to the average potential in the interstitial region. The correlation contribution to the crystal potential is negative and increases in magnitude with increasing density, being roughly proportional to  $\ln[n(\vec{r})]$  inside the muffin-tin-sphere [see Eq. (3a)]. Comparing with Figs. 2 and 3, structure in Figs. 6 and 7 can be seen to correlate with structure in the radial dependence of the self-consistent charge densities. It is also clear from Figs. 6 and 7 that we would expect the NR potential to place  $d$ -like valence states, which have much of their weight inside the muffin-tin spheres, lower in energy relative to the

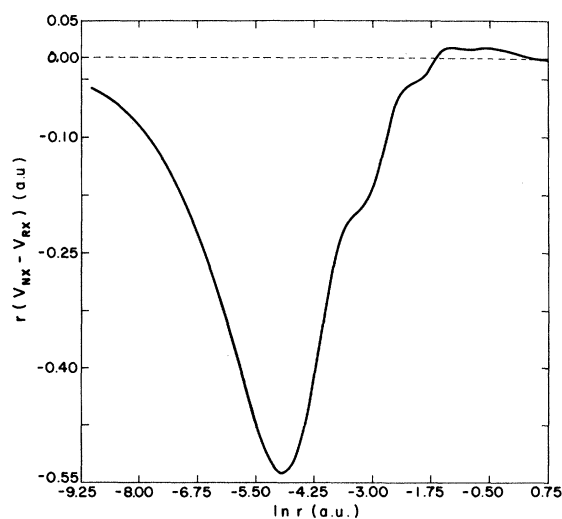


FIG. 9. Influence of the relativistic exchange correction on the self-consistent crystal potential of Pt.

*s-p*-like valence states than the HF potentials.

The influence of the relativistic exchange correction on the self-consistent crystal potentials for Pd and Pt is shown in Figs. 8 and 9. As expected, this correction is less important than the correlation correction for the lower-density region near the outer edge of the muffin-tin sphere but becomes more important as the extremely high-density region near the nucleus is approached. As a result we would expect the correlation contribution to have a larger impact on valence levels while the relativistic exchange correction should have a larger impact on the inner core levels.

### C. Single-particle energies

We first discuss our results for the core-level single-particle energies tabulated in Table II. As expected from Figs. 7 and 9 the correlation correction lowers (increases the magnitude of) the core energies while the relativistic exchange correction usually raises them (decreases the magnitudes). Also, as would be anticipated by comparing Figs. 6 and 7 with Figs. 8 and 9, the influence of the relativistic exchange correction is much larger than the influence of correlation for the innermost core levels. In fact, even for the outer core levels the two influences on the core energies are comparable. Everything else being constant, the relativistic exchange correction shows a tendency to decrease in magnitude with increasing principal quantum number ( $n$ ), orbital angular momentum ( $l$ ), and total angular momentum ( $j$ ). The correlation correction is much less sensitive to the  $l$  and  $j$  character of the core levels since it changes less rapidly with density. A particularly dramatic example of this sensitivity occurs for Pt where the signs of the relativistic exchange corrections in the  $4f$  and  $5s, 5p$  levels differ. In fact, at first sight, the sign of the relativistic exchange correction for the  $4f$  level is surprising. The direct effect of this correction is to make a repulsive contribution to the potential which increases sharply in magnitude near the nucleus. This in turn leads to a decrease in electron density near the nucleus and thus to a decreased screening to the nuclear charge at any given radius. The indirect attractive contribution dominates at some radii (see Figs. 7 and 8). Because of their high  $l$  character the  $f$  wave functions do *not* sample the direct repulsive relativistic exchange correction, and as a result, become more strongly bound when relativistic exchange is included. In contrast the binding of the  $4s, p$ , and  $d$  orbitals is reduced, because, although these orbitals have their principal maxima in the same region, they penetrate further into the core region. From these comparisons we see that the relativistic exchange

TABLE II. Core-level single-particle energies for Pd and Pt. The column headed by  $-E_{NR}$  gives the energy obtained with the NR exchange approximation while those headed by  $E_{RX} - E_{NX}$  and  $E_{HF} - E_{NX}$  give the shifts due to relativistic exchange corrections and correlation, respectively. All energies are in Ry.

$(n, l, j)$	Pd		
	$-E_{NR}$	$E_{RX} - E_{NR}$	$E_{HF} - E_{NX}$
$(1, 0, \frac{1}{2})$	1772.0	7.9	0.0
$(2, 0, \frac{1}{2})$	258.3	0.86	0.08
$(2, 1, \frac{1}{2})$	239.7	0.56	0.08
$(2, 1, \frac{3}{2})$	228.0	0.47	0.08
$(3, 0, \frac{1}{2})$	46.03	0.141	0.054
$(3, 1, \frac{1}{2})$	38.68	0.075	0.054
$(3, 1, \frac{3}{2})$	36.64	0.061	0.054
$(3, 2, \frac{3}{2})$	23.57	0.009	0.057
$(3, 2, \frac{5}{2})$	23.16	0.007	0.054
$(4, 0, \frac{1}{2})$	5.635	0.024	0.029
$(4, 1, \frac{1}{2})$	3.351	0.010	0.028
$(4, 1, \frac{3}{2})$	3.017	0.008	0.028
$(n, l, j)$	Pt		
	$-E_{NR}$	$E_{RX} - E_{NR}$	$E_{HF} - E_{NX}$
$(1, 0, \frac{1}{2})$	5750.0	38.6	0.2
$(2, 0, \frac{1}{2})$	1009.0	5.5	0.1
$(2, 1, \frac{1}{2})$	967.0	4.72	0.11
$(2, 1, \frac{3}{2})$	840.1	3.08	0.10
$(3, 0, \frac{1}{2})$	236.2	1.14	0.07
$(3, 1, \frac{1}{2})$	217.4	0.84	0.07
$(3, 1, \frac{3}{2})$	189.6	0.58	0.07
$(3, 2, \frac{3}{2})$	158.2	0.26	0.07
$(3, 2, \frac{5}{2})$	152.2	0.23	0.07
$(4, 0, \frac{1}{2})$	50.01	0.261	0.055
$(4, 1, \frac{1}{2})$	42.05	0.186	0.055
$(4, 1, \frac{3}{2})$	35.39	0.111	0.055
$(4, 2, \frac{3}{2})$	22.34	0.028	0.053
$(4, 2, \frac{5}{2})$	21.10	0.021	0.052
$(4, 3, \frac{5}{2})$	4.414	-0.024	0.049
$(4, 3, \frac{7}{2})$	4.159	-0.025	0.049
$(5, 0, \frac{1}{2})$	6.589	0.045	0.033
$(5, 1, \frac{1}{2})$	4.038	0.026	0.031
$(5, 1, \frac{3}{2})$	2.923	0.014	0.029

correction can have a greater influence on physical properties than the correlation potential. This should be especially true for crystals or molecules

TABLE III. Bottom, center, and top of  $s$ ,  $p$ , and  $d$  bands ( $E_b$ ,  $E_c$ ,  $E_t$ ) for Pd and Pt. Results are given for the NX potential and for correlation and relativistic corrections.

Band		Pd			Pt		
		NX	RX-NX	HF-NX	NX	RX-NX	HF-NX
$s_{1/2}$	$E_b$	0.013	0.003	0.008	-0.090	0.007	0.007
	$E_c$	0.385	0.004	0.007	0.257	0.008	0.008
	$E_t$	2.057	0.004	0.015	1.791	0.008	0.016
$p_{1/2}$	$E_b$	0.556	0.003	0.006	0.474	0.006	0.007
	$E_c$	1.296	0.004	0.008	1.184	0.008	0.009
	$E_t$	3.003	0.005	0.014	2.817	0.010	0.015
$p_{3/2}$	$E_b$	0.614	-0.002	0.006	0.667	-0.004	0.007
	$E_c$	1.369	0.002	0.008	1.434	0.007	0.009
	$E_t$	3.150	0.003	0.014	3.317	0.009	0.015
$d_{3/2}$	$E_b$	0.146	0.000	0.017	0.126	0.000	0.016
	$E_c$	0.359	0.000	0.019	0.381	-0.001	0.019
	$E_t$	0.527	0.000	0.023	0.599	-0.001	0.024
$d_{5/2}$	$E_b$	0.173	0.000	0.016	0.199	0.001	0.016
	$E_c$	0.396	0.000	0.020	0.487	-0.001	0.020
	$E_t$	0.571	0.000	0.023	0.735	-0.002	0.023

containing rare earths since  $spd$ - $f$  shifts frequently have a large impact.

We now turn to a discussion of the results for the valence levels. The first question one asks about the results is a very crude one: How are the relative band positions and bandwidths changed? To examine this, we consider only the muffin-tin part of the potential in a spherical Wigner-Seitz treatment.<sup>27</sup> The approximate bottom of the band occurs where the radial solution has zero derivative at the Wigner-Seitz radius,  $R_{WS}$ , the approximate top where the radial solution has zero value, and the approximate middle where the logarithmic derivative has the value  $-(l+1)/R_{WS}$ . We have tabulated these energies for Pd and Pt in Table III. Before comparing the results for the different xc potentials we make two general observations concerning the information presented. First, in using these indices we are, for the moment, ignoring the hybridization effects that have been so laboriously included in the calculation, except as they affect the muffin-tin component of the potential through energy shifts. These are only important when one is looking at a finer gauge. Secondly, we have solved the radial Dirac equation to obtain these indices so that we have separate results for  $j=l\pm\frac{1}{2}$ . The separation of these energies for  $j=l\pm\frac{1}{2}$  is roughly the spin-orbit splitting.

From Table III we see that the spin-orbit splitting is larger for the  $p$  band than for the  $d$  band and larger for Pt than for Pd. These results are expected since Pt has a larger nuclear charge and since the  $p$  orbitals penetrate closer to the nucleus. Further, the splitting increases in size as one goes from the bottom to the top of the band,

again because the wave functions at the top of the band penetrate closer to the nucleus. For Pt we note that the spin-orbit splitting at the top of the  $d$  band is a significant fraction of the full  $d$ -band width. This larger splitting is responsible for the partial separation of  $d_{3/2}$  and  $d_{5/2}$  bands in Pt noted previously by Christensen.<sup>28</sup> It also has the potential to cause inaccuracies in single-particle energies calculated using the method of Ref. 11. This point is discussed later.

The correlation correction lowers the  $d$  band relative to the  $s$  band for both Pd and Pt. This is because the attractive correlation contribution to the xc potential is larger in magnitude in the higher-density core region and is consistent with

TABLE IV. Influence of xc potential on some representative valence-level eigenvalues. For the HF and RX potentials the eigenvalues are given relative to the corresponding NR potential eigenvalues. The energies are given in mRy.

	NR		HF		RX	
	Pd	Pt	Pd	Pt	Pd	Pt
$\Gamma(1)$	13	-90	7	8	3	6
$X(5)$	575	743	24	28	0	0
$X(1)$	141	134	16	17	0	0
$\Gamma_5^+(2,3)$	318	344	21	23	0	0
$\Gamma_7^+(4)$	341	415	20	22	0	0
$\Gamma_9^+(5,6)$	451	552	23	26	0	0
$L(3)$	337	407	21	22	0	0
$L(4)$	532	634	24	27	0	0
$L(5)$	546	646	24	28	0	0

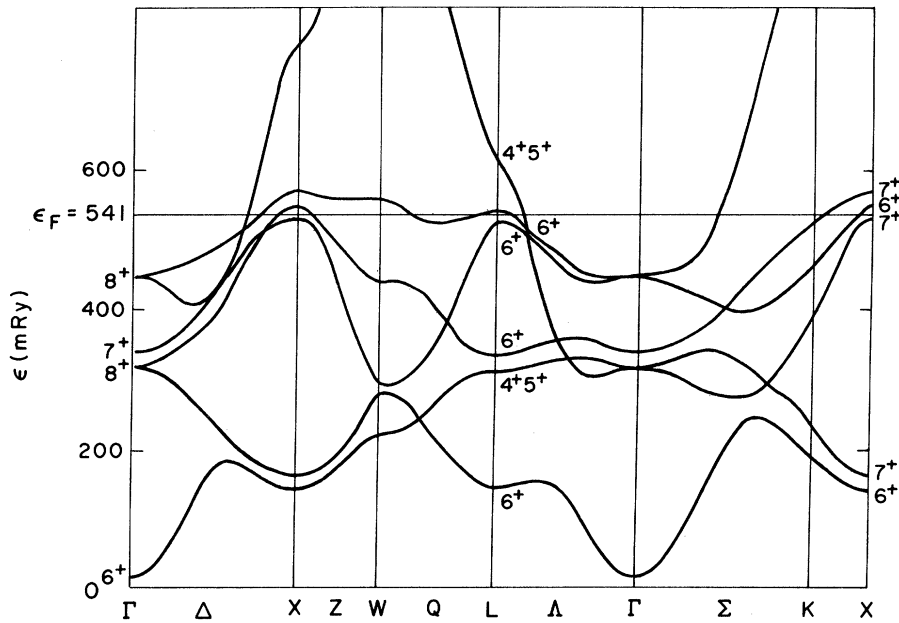


FIG. 10. Energy bands along high-symmetry lines for Pd with spin-orbit interactions included. The linearized APW energy parameter  $\epsilon_l$  was set to 0.2 Ry for this calculation.

Figs. 6 and 7. The bands are also narrowed by the correlation correction since the lowering is larger for the more localized orbitals near the top of the bands. The relativistic exchange correction raises the  $d$  band relative to  $s$  and  $p$  for both Pd and Pt. The  $s$  and  $p$  valence bands are raised due to the penetration of their core-ortho-

gonalization components near the nucleus. The corrections tend to be larger for Pt as expected. The near-zero change for the  $d$  bands is due, in part, to a cancellation between the positive and negative regions shown in Figs. 8 and 9. For Pd the relativistic exchange correction lowers the  $d$  band by 3 mRy relative to the  $s$  bands, and the

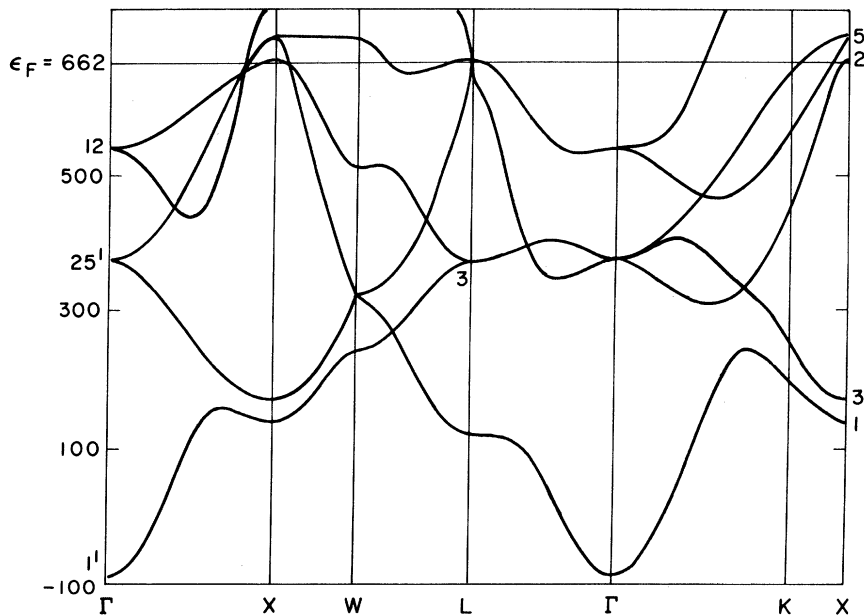


FIG. 11. Energy bands along high-symmetry lines for Pt with spin-orbit interactions neglected. The linearized APW energy parameter  $\epsilon_l$  was set to 0.4 Ry for this calculation.

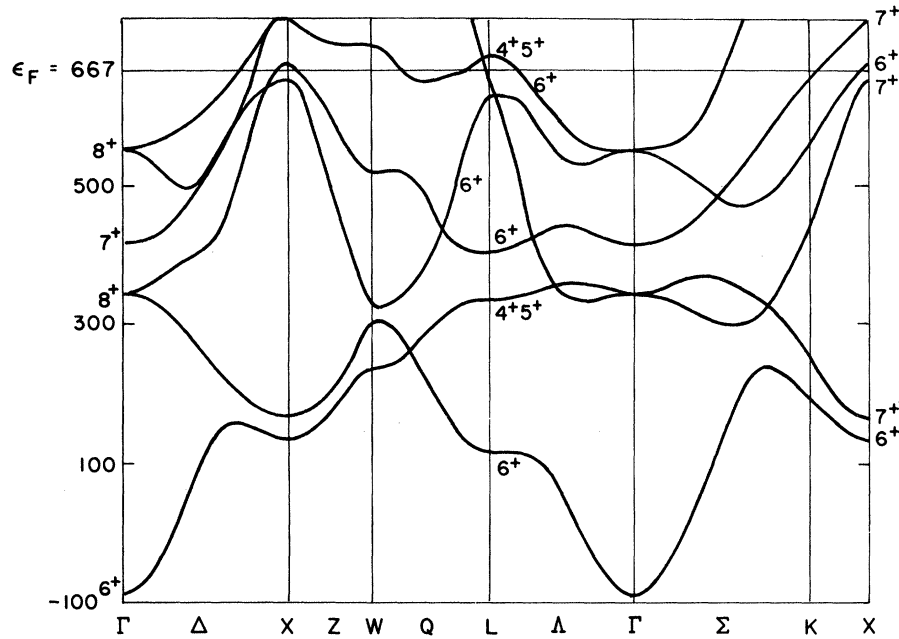


FIG. 12. Energy bands along high-symmetry lines for Pt with spin-orbit interactions included. The linearized APW energy parameter  $\epsilon_l$  was set to 0.2 Ry for this calculation.

correlation contribution lowers them by a further 12 mRy. For Pt the relative energy changes are 8 mRy and 12 mRy for relativistic exchanges and

correlation contributions, respectively. It is perhaps surprising that even for the valence levels of heavy metals the relativistic exchange correc-

TABLE V. Some representative eigenvalues for Pd and Pt, obtained with and without spin-orbit interaction corrections. For Pt, eigenvalues obtained using the full RAPW method are also listed. All results are for the HF potential. The LAPW energy parameters were  $\epsilon_l = 0.4$  for Pt and  $\epsilon_l = 0.2$  for Pd.

Metal	$\vec{k}$	Approx.	Band 1	Band 2	Band 3	Band 4	Band 5	Band 6
Pd	$\Gamma$	-SO	20	348	348	348	471	471
Pd	$\Gamma$	+SO	20	339	339	361	474	474
Pd	X	-SO	157	181	562	586	586	797
Pd	X	+SO	157	180	558	578	599	796
Pd	W	-SO	238	307	307	463	585	1219
Pd	W	+SO	237	302	310	464	586	1205
Pd	L	-SO	162	346	346	562	562	625
Pd	L	+SO	162	333	358	556	570	625
Pd	K	-SO	207	250	413	492	551	1086
Pd	K	+SO	206	249	412	492	552	1085
Pt	$\Gamma$	-SO	-82	339	399	399	565	565
Pt	$\Gamma$	+SO	-82	367	367	437	578	578
Pt	$\Gamma$	RAPW	-82	364	364	435	575	575
Pt	X	-SO	154	190	693	729	729	808
Pt	X	+SO	151	186	681	705	771	799
Pt	X	RAPW	150	184	671	693	762	789
Pt	W	-SO	260	343	343	534	727	1206
Pt	W	+SO	255	328	346	541	730	1206
Pt	W	RAPW	254	325	344	540	721	1193
Pt	L	-SO	134	396	396	641	694	694
Pt	L	+SO	132	357	429	641	674	719
Pt	L	RAPW	131	353	427	633	663	715
Pt	L	+SO	215	275	470	589	675	1100
Pt	K	+SO	211	269	463	589	684	1098
Pt	K	RAPW	209	268	459	584	678	1091

TABLE VI. Influence of relativistic and non-muffin-tin corrections on the relative position of  $s$  and  $d$  bands and on the  $d$ -band width in Pd ( $-SO$ ), ( $-R$ ), and ( $-NMT$ ) indicate results obtained with the omission of spin-orbit effects, all relativistic effects, and non-muffin-tin plus spin-orbit effects, respectively.  $X_{7^+} - X_{6^+}$  is a measure of the  $d$ -band widths while  $X_{7^+} - \Gamma_{6^+}$  and  $X_{6^+} - \Gamma_{6^+}$  are the energies to the bottom of the  $s$  band, respectively. These results were obtained with the NX potential.

Approx.	$X_{7^+} - X_{6^+}$	$X_{7^+} - \Gamma_{6^+}$	$X_{6^+} - \Gamma_{6^+}$
+ SO	432	557	125
-SO	419	545	126
-R	436	514	78
-NMT	431	546	115

tions, which represent quantum-electrodynamical corrections to the Coulomb interaction, are comparable with the correlation corrections to the band separations.

These qualitative observations are consistent with the detailed eigenvalue calculations. Some representative eigenvalues are listed in Table IV. The energy bands along high-symmetry lines in the crystal are shown in Figs. 10-12 for Pd with spin-orbit interactions, Pt without spin-orbit interactions, and Pt with spin-orbit interactions, respectively. The influence of the spin-orbit interaction on some representative eigenvalues is shown in Table V by presenting eigenvalues obtained with and without the spin-orbit interaction.

(The eigenvalues without spin-orbit interaction corrections are readily available since they appear as an intermediate quantity in the method of Ref. 11.) For Pt we also present eigenvalues obtained with the full RAPW method. For Pd we note that the spin-orbit interaction has little influence on eigenvalues except for those cases in which it lifts a degeneracy. In contrast, even nondegenerate eigenvalues are significantly shifted in Pt. This extra feature is due to the aforementioned  $d_{5/2} - d_{3/2}$  separation in Pt. The  $d_{5/2} - d_{3/2}$  separation also is partly responsible for the eigenvalue differences between the RAPW method and the method of Ref. 11 as shown in Table V. The remaining discrepancy can be attributed to the linearization. It should be noted that these differences are not large for eigenvalues with a value near the energy parameter. (As was pointed out in Ref. 11, the corresponding differences are  $\sim 1$  mRy in Pd over the entire  $d$  band.) Despite the significant  $d^{3/2} - d^{5/2}$  separation we would not expect the inclusion of spin-orbit interactions at the self-consistency iteration stage to greatly influence the self-consistent potential for Pt. This is because the Fermi level lies above both the more- $d^{3/2}$ -like and the more- $d^{5/2}$ -like parts of the  $d$  band. The semirelativistic  $d$ -wave function should therefore be an appropriate average for the occupied portion of the  $d$  bands. For metals nearer the middle of the  $5d$  series, inclusion of

TABLE VII. Symmetry-point eigenvalues for the NX potential for Pd and Pt. Energies are given relative to the Fermi level. For Pd the energies at  $\Gamma$  and  $L$  are compared with experiment. All energies are given in mRy.  $E_F = 541$  for Pd and  $E_F = 667$  for Pt (see Sec. IVD).

	Band 1	Band 2	Band 3	Band 4	Band 5	Band 6
Pd						
$\Gamma$	-528	-223	-223	-200	- 90	- 90
$\Gamma_{\text{expt}}^a$		-188 $\pm$ 11	-188 $\pm$ 11	-188 $\pm$ 11	- 85 $\pm$ 7	- 85 $\pm$ 7
$X$	-400	-379	- 7	13	34	247
$K$	-352	-309	-148	- 71	- 12	531
$L$	-395	-229	-204	- 9	5	78
$L_{\text{expt}}^a$		-176 $\pm$ 15	-176 $\pm$ 15	- 29 $\pm$ 15	- 7 $\pm$ 7	
$W$	-321	-257	-249	- 99	21	652
Pt						
$\Gamma$	-757	-323	-323	-252	-115	-115
$\Gamma_{\text{expt}}^b$		-299	-299	-206	-105	-103
$X$	-533	-500	- 14	9	76	124
$K$	-475	-416	-223	-103	- 10	417
$L$	-551	-333	-260	- 33	- 21	24
$W$	-430	-360	-340	-148	34	522

<sup>a</sup>Experimental values from Ref. 30.

<sup>b</sup>Experimental values from Ref. 31.

spin-orbit interactions could be more important in determining the self-consistent crystal potential.

It is interesting to isolate the influences of other relativistic and non-muffin-tin corrections which would not be included in more simplified band-structure calculations. In addition to spin-orbit interactions, relativistic corrections come from mass-velocity and Darwin terms.<sup>29</sup> Both these terms introduce a negative shift in the single-particle eigenvalues; the Darwin term shifts  $s$  levels only while the mass-velocity term is larger for the higher kinetic energy  $d$  bands than for the  $sp$  bands. The total effect of both terms is a shift of the  $sp$  band downward relative to the  $d$  band, and a narrowing of the  $d$  band. Detailed results for Pd are given in Table VI. Note that the  $d$ -band narrowing mentioned above, 17 mRy for Pd, is compensated for by a broadening due to spin-orbit splitting of some levels near the top of the  $d$  band. Also indicated in Table VI is the size of corrections due to non-muffin-tin terms in the crystal potential. These changes are less systematic than the relativistic changes, and for both Pd and Pt are fairly small, typically  $\sim 5$  mRy.

Finally, in Table VII we compare our calculated eigenvalues with those obtained by Himpfel and Eastman<sup>30</sup> for Pd and Mills *et al.*<sup>31</sup> for Pt using angle-resolved photoemission. The theoretical eigenvalues are sometimes outside experimental

error bars by as much as 30 mRy and the size of discrepancy is larger in magnitude than corrections introduced by non-muffin-tin corrections or the choice of xc potential. The discrepancy gives the appearance that the "experimental  $d$  bands" are narrower than the calculated ones. This is precisely the same situation as found for nickel<sup>32</sup> where it has received considerable attention (including questioning of the effect<sup>33</sup>). However, as this is really an excitation property which raises questions of relaxation and lifetime effects, we shall not attempt to resolve this discrepancy. Should the lifetime and relaxation effects be resolved, the interesting fundamental question of the accuracy of the single-particle equations as used here for eigenvalues away from the Fermi energy could be addressed.<sup>34</sup> Even so, we note one other anomaly which can be related to the  $L$ -level disparity observed in Ni. In Pd, the fifth-band  $L$ -centered hole pocket observed in de Haas-van Alphen measurements is inconsistent with placing the fifth band below the Fermi surface at  $L$ . Thus we see a discrepancy in the interpretation of two experimental measurements. As the calculations concur with the de Haas-van Alphen measurements<sup>35</sup> (which, after all, involve the more weakly interacting probe), the problem is most likely in the interpretation of the photoemission experiment.

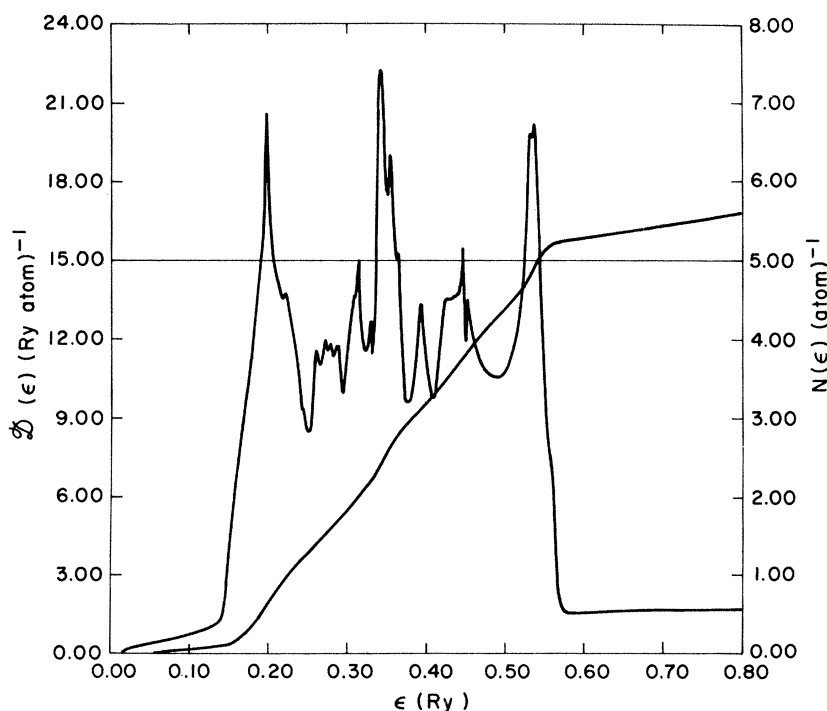


FIG. 13. Density of states and number of occupied states below energy  $\epsilon$  for Pd with spin-orbit interaction.

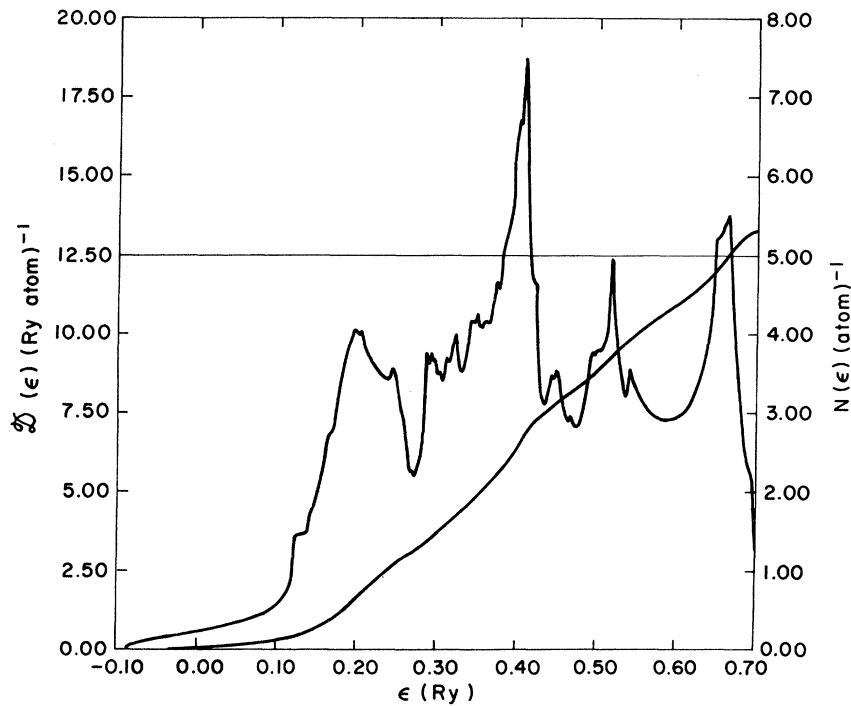


FIG. 14. Density of states and number of occupied states below energy  $\epsilon$  for Pt without spin-orbit interaction.

#### D. Energy-derived properties

In this section we discuss our results for a number of properties calculated directly from the va-

lence-level eigenvalues. Extremal areas and cyclotron masses, which can be compared in detail with de Haas-van Alphen experiments, will be discussed separately. The number of occupied

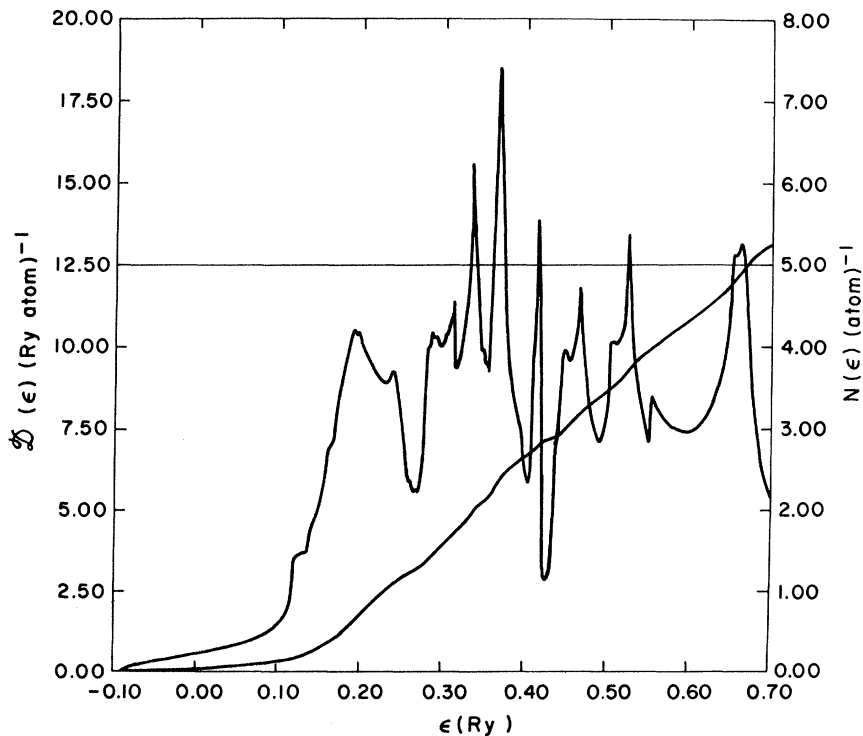


FIG. 15. Density of states and number of occupied states below energy  $\epsilon$  for Pt with spin-orbit interaction.

TABLE VIII. Partial occupations and densities of states from 4th, 5th, and 6th bands of Pd and Pt.  $N_i(E_F)$  is given in units of electrons per (atomic spin) while  $D_i(E_F)$  is given in units of electrons per (Ry atom spin).

Metal	Potential	$E_F$	$N_4(E_F)$	$N_5(E_F)$	$D_6(E_F)$	$D_4(E_F)$	$D_5(E_F)$	$D_6(E_F)$	$D(E_F)$
Pd	HF	564	0.997	0.811	0.192	0.38	15.53	1.76	17.67
Pd	NR	540.1	0.997	0.815	0.187	0.38	15.37	1.69	17.45
Pd	RX	540.1	0.997	0.816	0.187	0.39	15.30	1.67	17.36
Pt	HF	689.8	0.9997	0.790	0.210	0.08	9.73	2.07	11.88
Pt	NR	663.7	0.9998	0.792	0.208	0.07	10.28	2.02	12.37
Pt	RX-SO	659.2	0.997	0.773	0.230	0.26	11.77	1.93	13.96
	RX+SO	663.3	0.9998	0.792	0.208	0.07	0.20	2.04	12.31

states and the density of states,  $N(\epsilon)$  and  $D(\epsilon)$  [Eqs. (6) and (7)], are given as a function of energy in Figs. 13–15 for Pd, Pt without spin-orbit interactions, and Pt with spin-orbit interactions. The width of the  $d$  band of Pd, as seen from the  $D(\epsilon)$  curve, is 0.46 Ry compared to 0.60 Ry in Pt. Correspondingly, the  $d$ -band density of states in Pd is typically higher than in Pt. For Pt we note that the inclusion of the spin-orbit interaction introduces considerable extra structure in the density-of-states curve. The densities of states and partial occupations for the 4th, 5th, and 6th bands at the Fermi level for Pd and Pt are given in Table VIII. For Pd, the lowering of the  $d$  band when correlation is included, moves the Fermi level farther from the sharp peak in  $D(\epsilon)$  and thereby reduces  $D(\epsilon_F)$  even though the  $d$  band is slightly narrowed. For Pt the corresponding peak in  $D(E)$  is not as sharp and correlation in-

creases  $D(\epsilon_F)$ . We note that if we had neglected the spin-orbit interaction, the Fermi-level density of states would have been about 1% larger. In fact, as discussed later, the Fermi surface of Pt is significantly altered by the spin-orbit interaction.

In Fig. 16 we show  $\langle V^2(\epsilon) \rangle$  [Eq. (9)], as a function of  $E$  for Pt. In atomic units  $\langle V^2(\epsilon) \rangle = 4\epsilon$  for a free-electron system and we see, in the curve, free-electron-like regions both below the bottom of the  $d$  band and above the top of the  $d$  band. In the middle of the  $d$  band, energies of low average velocity are seen to correspond to peaks in the density-of-states curve while regions of high average velocity correspond to valleys. The information is presented in Fig. 16 and is useful in interpreting transport properties of these metals.<sup>36</sup> A similar correspondence between  $D(\epsilon)$  and  $\langle V^2(\epsilon) \rangle$  curves was obtained for Pd.

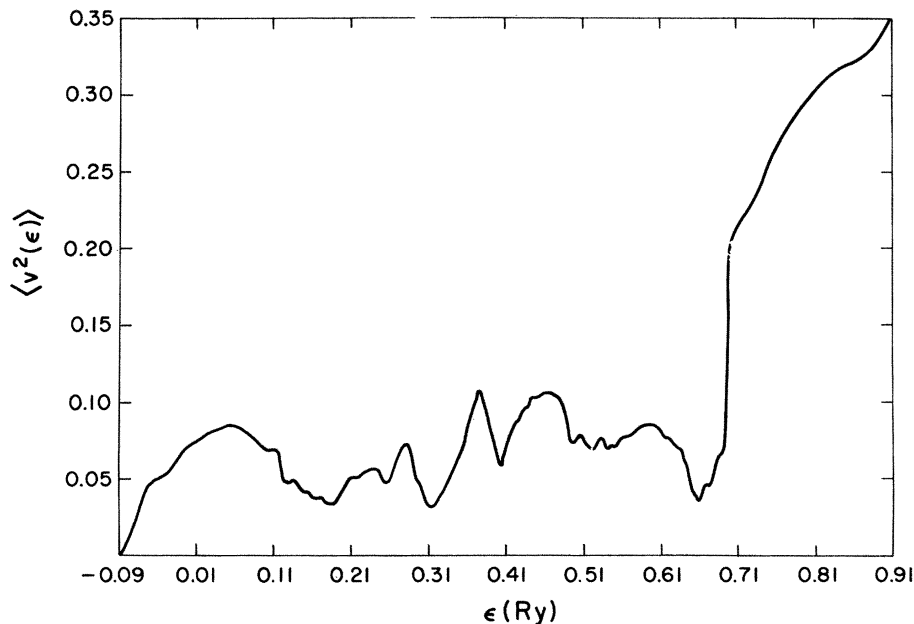


FIG. 16.  $\langle V^2(\epsilon) \rangle$  as a function of energy for Pt. Local minima in this curve correspond approximately to local maxima in the  $D(\epsilon)$  curve for Pt (Fig. 15).  $V_{\vec{k}} = \nabla \epsilon_{\vec{k}}$  was calculated using energies in Ry and wave vectors in units of  $(\pi/a)$ .

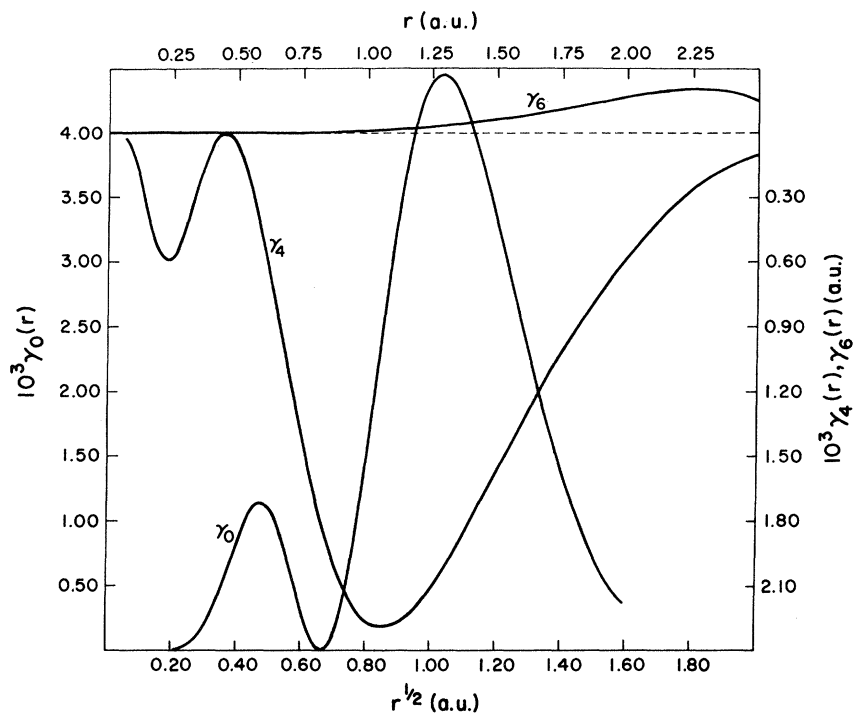


FIG. 17. Induced magnetization density distribution for Pd. The upper scale and right-hand scale refer to the  $\gamma_0(r)$  curve while the lower and right-hand scales refer to the  $\gamma_4(r)$  and  $\gamma_6(r)$  curves.

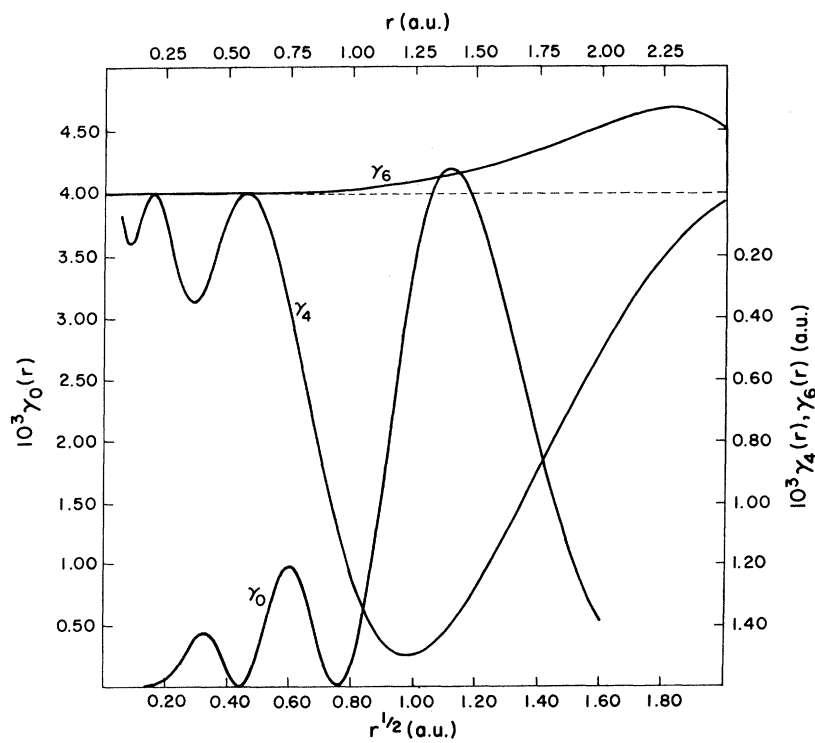


FIG. 18. Induced magnetization density distribution for Pt. The upper scale and right-hand scale refer to the  $\gamma_0(r)$  curve while the lower and right-hand scales refer to the  $\gamma_4(r)$  and  $\gamma_6(r)$  curves.

## E. Magnetic properties

The Fermi-surface charge densities  $\gamma(\vec{r})$  [Eq. (10)], for Pd and Pt are shown in Figs. 17 and 18. As mentioned previously, the magnetization induced in Pd or Pt by a constant magnetic field is expected to be nearly proportional to  $\gamma(\vec{r})$ . The qualitative features of  $\gamma_0(r)$ ,  $\gamma_4(r)$ , and  $\gamma_6(r)$  are similar to those of the radial functions appearing in the expansion of the charge density,  $\sigma_0(r)$ ,  $\sigma_4(r)$ , and  $\sigma_6(r)$ . Much of the discussion given for that case applies here as well, but one important difference should be noted. On the average,  $\gamma(r)$  is more anisotropic inside the muffin-tin sphere

than  $n(r)$ . This feature has two causes. Firstly at smaller values of  $r$ ,  $n(r)$  is dominated by the spherically symmetric contribution from the core electrons. Secondly, even at larger values of  $r$ , the anisotropy of the total contribution to the density from *one* energy tends to be larger than the anisotropy of the total contribution from *all* occupied energies. We shall see that this anisotropy of the induced magnetization of Pd and Pt makes a contribution to the magnetic susceptibility of these materials.

The form factors of the induced magnetization [Eq. (12)] are presented and compared with experiment.<sup>37,38</sup> We note that the magnitude of the form

TABLE IX. Comparison of theoretical and experimental magnetic form factors for Pd and Pt. The subscript "MT" is used to denote results obtained using the muffin-tin approximation for the induced magnetization. Differences in form factors for electrons corresponding to reciprocal-lattice vectors of the same magnitude reflect primarily the anisotropy of the induced magnetization inside the muffin-tin sphere. We compare results here with previous calculations.

$(hkl)$	Pd <sub>MT</sub>	$\gamma(G)/\gamma(0)$ Theory		Pt	$\gamma(G)/\gamma(0)$ Experiment	
		Pd	Pt <sub>MT</sub>		Pd <sup>a</sup>	Pt <sup>b</sup>
(000)	1.000	1.000	1.000	1.000	1.000	1.000
(111)	0.484	0.488	0.404	0.408	0.536 ± 0.015	0.444 ± 0.036
(200)	0.382	0.373	0.295	0.288	0.433 ± 0.015	0.360 ± 0.036
(220)	0.133	0.138	0.051	0.055	0.178 ± 0.015	0.084 ± 0.027
(311)	0.047	0.041	-0.015	-0.019	0.035 ± 0.018	0.077 ± 0.042
(222)	0.030	0.048	-0.026	-0.012	0.070 ± 0.018	0.000 ± 0.057
(400)	-0.009	-0.047	-0.038	-0.068	-0.077 ± 0.015	-0.109 ± 0.054
(331)	-0.018	-0.026	-0.033	-0.021	0.006 ± 0.018	
(420)	-0.019	-0.027	-0.030	-0.035	-0.045 ± 0.025	
(422)	-0.019	-0.011	-0.018	-0.014	0.035 ± 0.015	
(511)	-0.017	-0.040	-0.010	-0.026	-0.043 ± 0.015	
(333)	-0.017	0.005	-0.010	0.002	0.020 ± 0.015	
(440)	-0.010	-0.001	-0.002	0.007		
(531)	-0.005	-0.003	0.007	0.008		
(600)	-0.003	-0.034	0.009	-0.009		
(442)	-0.003	0.011	0.009	0.018		
(620)	0.003	-0.012	0.015	0.007		
(533)	0.007	0.018	0.018	0.025		
(622)	0.008	0.003	0.01	0.017		
(444)	0.013	0.028	0.023	0.030		
(711)	0.017	0.000	0.024	0.017		
(511)	0.017	0.023	0.024	0.027		
(640)	0.018	0.019	0.025	0.026		
(624)	0.021	0.025	0.026	0.027		
(731)	0.023	0.018	0.026	0.024		
(553)	0.023	0.031	0.026	0.028		
	Pd <sub>w</sub> <sup>c</sup>	Here	Pt <sub>w</sub> <sup>d</sup>	Here		
(511)-(333)	-0.018	-0.045	-0.134	-0.028	-0.063	
(600)-(442)	-0.077	-0.045	-0.124	-0.027		
(711)-(551)		-0.023		-0.010		
(731)-(553)		-0.013		-0.004		

<sup>a</sup>Reference 37.

<sup>b</sup>Reference 38.

<sup>c</sup>Theoretical results in Ref. 39.

<sup>d</sup>Theoretical results in Ref. 40.

factor decreases less rapidly with increasing reciprocal-lattice vector magnitude for Pd than for Pt. This reflects the more localized nature of the 4d induced magnetization in Pd compared to the 5d induced magnetization in Pt and is consistent with Figs. 17 and 18. Some pairs of reflection planes correspond to reciprocal-lattice vectors of different symmetry but the same magnitude. In the muffin-tin approximation the form factors would be the same for each member of such a pair so that any calculated differences are a direct reflection of the non-muffin-tin components of  $\gamma(r)$ . The calculated form factors indicate that the non-muffin components have similar shapes for Pd and Pt with the magnitude being larger for Pd. This is again consistent with Figs. 17 and 18. In comparing theoretical and experimental form factors, it should be remembered that differences can be due to valence- and core-polarization contributions to the spin-induced magnetization density or orbital contributions to the induced magnetization. In addition, we have not included  $g$  shifts in this calculation, and to be consistent have not included the spin-orbit interaction in calculating  $\gamma(r)$ . (This point is discussed in more detail below.) As a result, it is not possible to assign the differences between theory and experiment seen in Table IX to a single source. However, from the level of agreement we can conclude that the spin-induced magnetization dominates for both metals. The comparison of the theoretical and experimental predictions of the size of non-muffin-tin components of the induced magnetization is also interesting. For Pd the experimental result is midway between our result and the non-self-consistent field warped muffin-tin (WMT) results,<sup>39</sup> with both theoretical predictions lying within experimental error bounds. As mentioned previously, and in contradiction with earlier results (see Table IX), our calculation shows a decrease in the non-muffin-tin component in going from Pd to Pt. Because Maglic *et al.*,<sup>38</sup> have not measured form factors for the (511) and (333) reflection planes, we make contact with experimental measurements of

the magnetization anisotropy via the crystal-field model of Weiss and Freeman.<sup>41</sup> In this model the symmetry is due to the difference of the fractional  $e_z$  population for the magnetic electrons,  $\gamma$ , from the value  $\frac{2}{5}$  required for spherical symmetry. By fitting to their experimental results using this model, Maglic *et al.* obtain  $\gamma = 0.30 \pm 0.17$ . From the differences listed in Table IX, we obtain  $\gamma = 0.30$ . This result is in excellent agreement with experiment, in contrast with the theoretical result  $\gamma = 0.07$  obtained previously by Watson-Yang *et al.*<sup>39</sup> This discrepancy can be understood in terms of the instability of the self-consistency process: one expects a non-self-consistent calculation to overshoot in the process of achieving self-consistency. The calculation of Watson-Yang *et al.* was an overlapping atomic-density calculation in the warped muffin-tin approximation that neglects the nonspherical terms inside the muffin-tin (MT) spheres. Clearly an overshoot in going from spherical symmetry would be expected to result in too much anisotropy.

Finally, in Table X, we present our results for the density-functional Stoner parameter,  $I$ , and the spin susceptibility. We note that including non-muffin-tin components in the charge density increases the Stoner parameter. The calculated results for the spin susceptibility support the usual assumption that this component dominates the total magnetic susceptibility for both Pd and Pt. In comparing with experiment, however, it must be remembered that we have not included  $g$  shifts in calculating our spin susceptibility. This point has been touched on previously in discussing the temperature dependence of  $\chi_p$  for Pd and Pt.<sup>15</sup> In fact, as has been emphasized by Misra and Kleinman,<sup>42</sup> the spin-orbit interaction influences the total magnetic susceptibility in several ways. The Pauli susceptibility term is modified by a factor,  $\langle g^2/4 \rangle$ , where the average is over the Fermi surface. The local  $g$  factors are related to matrix elements of the total magnetic-moment operator among the single-particle states at that point.<sup>43</sup> We have calculated  $\langle g^2/4 \rangle$  as a function of energy for Pd and

TABLE X. Spin susceptibilities and density-functional Stoner parameters for Pd and Pt.  $I$  is given in units of mRy and  $D(E_F)$  in electrons per (Ry atom).  $I_{MT}$  is the result obtained for  $I$  when the muffin-tin approximation for  $\gamma(r)$  is used. The calculated spin susceptibility and the experimental total susceptibility are given in units of  $10^{-6}$  (emu/mole).

Metal	Potential	$D(E_F)$	$I_{MT}$	$I$	$\chi_p$	$\chi^{expt}$
Pd	HF	35.3	25.9	26.7	14.60	
Pd	NR	34.9	25.9	26.7	12.20	
Pd	RX	34.7	25.9	26.7	11.20	720
Pt	HF	23.8	23.5	24.3	130	
Pt	NR	24.7	23.5	24.3	150	
Pt	RX	24.6	23.5	24.3	150	210

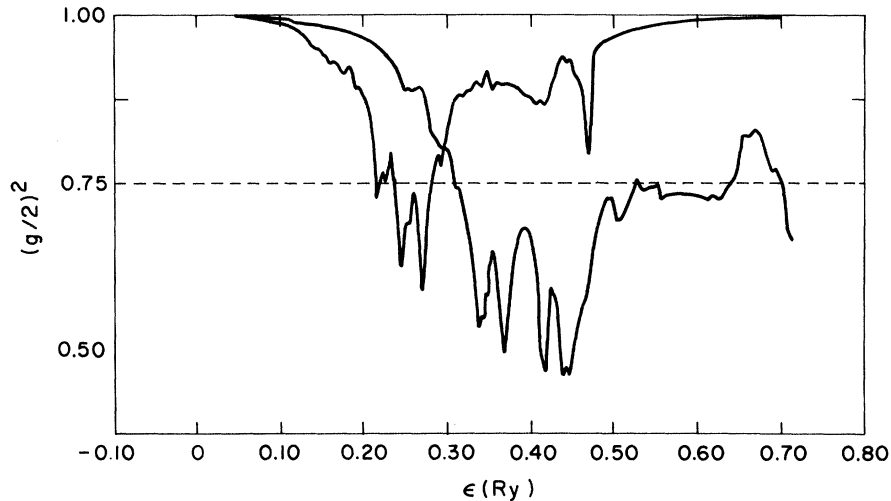


FIG. 19.  $\langle g^2(\epsilon)/4 \rangle$  as a function of energy for Pd and Pt (see text). The lower curve corresponds to Pt which has larger relativistic effects.

Pt, but using only the spin part of the magnetic-moment operator. The results are shown in Fig. 19. It can be shown<sup>15,14</sup> that these "spin-only"  $g$  shifts are related to the magnetic susceptibility for a fictional magnetic field which couples only to the spin magnetic moment of the electrons. The strong shifts in the middle of both Pd and Pt  $d$  bands demonstrate that "up-spins" and "down spins" are thoroughly mixed by the spin-orbit interaction in these metals. A proper calculation of the Pauli susceptibility in these metals ought to include a treatment of the full  $g$  shift. From Fig. 19 we see that this requirement is stronger for heavier metals and stronger in the middle of a given transition series. However, a formal treatment of the xc enhancement of the Pauli susceptibility in this case is, as yet, unavailable.

#### F. Fermi surface

To investigate the Fermi-surface properties we utilize an orbit-tracing package based on the standard relativistic APW method which evaluated  $dE/d\vec{k}$  by a Hellman-Feynman technique.<sup>21</sup> Because of the large masses found in Pd and Pt, it is important to reduce the numerical errors which can occur in the more approximate scheme used in the SCF and density-of-states calculations. This introduces the necessity that the Fermi energy be recalculated for the RAPW results. Rather than recalculate the density of states, we calculated the RAPW and the SO-LAPW eigenvalues at a number of representative  $\vec{k}$  points. For Pd, the correction was very small. The value of  $E_F$  used for the Pd-NX calculation presented in Table XI was 0.5408 Ry versus 0.5401 Ry from Table VIII. For Pt, RAPW vs SO-LAPW energy,

the shifts were larger and in addition there was about a 2-mRy variation in the shift to be applied. This indicates that the SO-LAPW would give a slightly different Fermi surface than the RAPW.

Table XI compares the areas obtained from the Pd-NX potential with experimental areas.<sup>35</sup> The Pd-R potential results are very nearly identical

TABLE XI. Pd Fermi-surface areas are compared for the NX potential with the experimental results given in Ref. 35. Units are a.u.<sup>-2</sup>.

$H$	$\Gamma$ -centered electron surface	
	$A$ (Theor.)	$A$ (Expt.)
$\langle 100 \rangle$	0.739	0.731
$\langle 110 \rangle$	0.839	0.827
$\langle 111 \rangle$	0.653	0.648
	Open surface holes	
$\langle 100 \rangle \alpha$	0.058	0.072
$\langle 100 \rangle \epsilon$	2.038	1.969 <sup>a</sup>
$\langle 110 \rangle \beta$	0.314	0.308 <sup>a</sup>
$84^\beta$	0.238	0.285
$63^\beta$	0.197	0.218
	$L$ -centered holes	
$\langle 100 \rangle$	0.0063	0.0061
$\langle 110 \rangle LKT$	0.0090	0.0088
$\langle 110 \rangle$	0.0063	0.0058
$\langle 111 \rangle LKW$	0.0053	0.0051
$\langle 211 \rangle LWI$	0.0087	0.0087
	$X$ -centered holes	
$\langle 100 \rangle XWT$	0.021	0.024
$\langle 110 \rangle$	0.021	0.024
$\langle 111 \rangle$	0.018	0.020

<sup>a</sup>Inferred from KKR fit.

with those of Pd-NX, indicating that the relativistic interactions have very little effect on the Fermi surface. Correlation, on the other hand, has a more dramatic effect. Because of the close proximity of two van Hove singularities in the  $d$  bands to the Fermi energy<sup>44</sup> (giving rise to the peaks in the density of states mentioned above), the Fermi energy is very tightly pinned in the  $d$  bands. Removing the correlations has the effect of raising the  $d$  bands relative to the  $sp$  bands (the same as decreasing  $\alpha$ ), and therefore raises the Fermi level in the  $sp$  bands. Thus the band 6  $\Gamma$ -centered electron surface which is already too large is further increased in size by the neglect of correlation. The implication is that the results would be improved by a stronger exchange-correlation (perhaps self-interaction correction) term. This is the same as found for copper.<sup>45</sup>

The astute observer will note a feature of some concern in Table XI: The theoretical electron surface is too large and most orbits on the open-hole surface show it to be too small. Parenthetically we might remark that all band-structure calculations find too small a value for the  $\alpha$  orbit. Has the Fermi energy been properly evaluated? The  $L$ -centered and  $X$ -centered ellipsoids are really too small to account for the apparent discrepancy. Its resolution appears to be revealed by the calculated  $\langle 110 \rangle \beta$  orbit being too large. Apparently, the calculated results give too large fins on the open-hole surface which is compensated by the electron surface bulging in the  $\langle 100 \rangle$  direction and the arms of the open-hole surface (jungle gym) being too small. A more detailed discussion of the Fermi surface is given in Ref. 35.

The case of Pt is more interesting for our purposes since, as can be seen from Table XII, the relativistic interactions are significant. In fact, the correlation effects and the relativistic interactions are nearly equal and opposite in sign, so

TABLE XII. Pt Fermi-surface areas are compared for the exchange only (HF), exchange-correlation (NX), and exchange-correlation plus relativistic interaction (RX) calculations with the experimental results (Ref. 46). Units are a.u.<sup>-2</sup>.

$H$	$\Gamma$ -centered electron surface			
	$A$ (HF)	$A$ (NX)	$A$ (RX)	$A$ (Expt.)
$\langle 100 \rangle$	0.765	0.743	0.761	0.770
$\langle 110 \rangle$	0.851	0.824	0.846	0.857
$\langle 111 \rangle$	0.684	0.665	0.678	0.678
	Open-hole surface			
$\langle 100 \rangle \epsilon$	1.931	1.883	1.922	1.890
$\langle 100 \rangle \alpha$	0.069	0.078	0.069	0.074

the RX results are very close to the HF results and both are generally closer to experiment than the NX (correlation only) results.

## V. SUMMARY AND CONCLUSIONS

We have solved the relativistic Kohn-Sham single-particle equations for Pd and Pt using xc potentials including exchange only (HF), exchange and correlation (NX), and exchange-correlation plus a relativistic exchange correction (RX). The solution of these band equations was elaborate in that many commonly adopted approximations were not used. A number of electron properties were calculated from the self-consistent eigenvalues and eigenspinors and these were examined for their sensitivity to the choice of xc potential and for their sensitivity to approximations made in solving the equations.

Of the quantities we have calculated, the electron-number density and magnetization density in an applied magnetic field would be given exactly if the exact xc energy functional were known. The results obtained for these functions were not very sensitive to the choice of xc potential (see Table I). However, for the anisotropy of the induced magnetization density, a large difference between our results and those of an earlier calculation based on the overlapping charge-density model was noted. In this case, we were able to compare with magnetic form factors deduced from neutron scattering and conclude that the self-consistent inclusion of nonmuffin terms in the effective potential resulted in a better description of the experiment.

The relationship of the Fermi surface obtained from Kohn-Sham eigenvalues to the experimental Fermi surface is formally only an approximation.<sup>34</sup> However, the Fermi surfaces obtained here were found to be very similar to the experimental surfaces (see Tables XI and XII). The inclusion of relativistic kinematics is essential to obtaining the qualitative features of the Fermi surface correctly, especially for Pt, but the non-muffin-tin terms included here with much effort are less important. On a quantitative level the relativistic exchange correction does improve the Fermi surface obtained for Pt but has little effect for Pd. In both cases, however, quantitative discrepancies exist between the RX Fermi surface and experiment.

For energies away from the Fermi surface, and the associated excitation energies of the solid, the limits of single-particle theory are well recognized. In fact, the situation noted for the photoemission is very reminiscent of that found in atomic structure: the photoemission results agree rather well with the calculations obtained using

the overlapping charge-density model and the full Slater exchange term, whereas our results yield wider  $d$  bands. This is precisely what was found for the atomic-structure calculations where the use of the full Slater exchange term mocked up relaxation effects in the eigenvalue differences. (On the other hand, Hartree-Fock energies calculated using orbitals obtained from  $\alpha = \frac{2}{3}$  SCF calculations also did quite well.) This effect persisted into the semiconductor SCF calculations where those using the full Slater exchange often gave a better representation of the optical spectrum.<sup>47</sup> On the other hand, we have focused on a *comparison* of the influences of correlation and relativistic-exchange contributions to the local potential on the eigenvalues (see Tables II, III, and IV), assuming that any conclusions drawn

here will carry over to more complete calculations of excitation energies. The relativistic exchange contribution was found to have a much larger impact than the correlation contribution for the core levels, the contributions of relativistic exchange and correlation are comparable even for the valence levels and in the case of Pt.

A good deal of effort has been spent on obtaining accurate forms for the correlation contribution to the effective potential.<sup>5</sup> (For example, see the recent analysis of Vosko *et al.*<sup>48</sup>) We suggest that the relativistic exchange correction, which is often equally important, should therefore be included when solving the relativistic Kohn-Sham equations, especially for systems containing atoms at the upper end of the Periodic Table.

\*Present address: Physics Department, McMaster University, Hamilton, L8S 4M1 Canada.

<sup>1</sup>O. K. Andersen, Phys. Rev. B 2, 883 (1970); J. Appl. Phys. 41, 1225 (1970); N. F. Berk and J. R. Schrieffer, Phys. Rev. Lett. 17, 433 (1966); S. Doniak and S. Engelsberg, *ibid.* 17, 750 (1966); F. M. Mueller, A. J. Freeman, J. O. Dimmock, and A. M. Furdyna, Phys. Rev. B 1, 4617 (1970); F. M. Mueller, A. J. Freeman, and D. D. Koelling, J. Appl. Phys. 41, 1229 (1970).

<sup>2</sup>For example, see O. Gunnarsson and B. I. Lundqvist, Phys. Rev. B 13, 4274 (1976).

<sup>3</sup>Results for all metals with atomic number less than 50 are presented in V. L. Moruzzi, J. F. Janak, and A. R. Williams, *Calculated Electronic Properties of Metals* (Pergamon, New York, 1978); The LDA and other improved approximations for  $E_x[n]$  are discussed by O. Gunnarsson, M. Jonson, and B. I. Lundqvist, Phys. Rev. B 20, 3136 (1979).

<sup>4</sup>A. H. MacDonald and S. H. Vosko, J. Phys. C 12, 2977 (1979); A. K. Rajagopal, *ibid.* 11, L943 (1978).

<sup>5</sup>W. Kohn and L. J. Sham, Phys. Rev. 140, A1133 (1965).

<sup>6</sup>For example, see J. D. Bjorken and S. D. Drell, *Relativistic Quantum Mechanics* (McGraw-Hill, New York, 1964).

<sup>7</sup>A. H. MacDonald, M. W. C. Dharma-wardana, and D. J. W. Geldart, J. Phys. F 10, 1719 (1980). This reference contains convenient parametrizations of xc potentials corresponding to a number of recent electron-gas calculations.

<sup>8</sup>O. Gunnarsson, B. I. Lundqvist, and J. W. Wilkins, Phys. Rev. B 10, 1319 (1974).

<sup>9</sup>O. K. Andersen, Phys. Rev. B 12, 3060 (1975).

<sup>10</sup>D. D. Koelling and G. O. Arbman, J. Phys. F 5, 2041 (1975).

<sup>11</sup>A. H. MacDonald, W. E. Pickett, and D. D. Koelling, J. Phys. C 13, 2675 (1980).

<sup>12</sup>N. Elyashar and D. D. Koelling, Phys. Rev. B 15, 3620 (1977).

<sup>13</sup>N. Elyashar and D. D. Koelling, Phys. Rev. B 13, 5362 (1976).

<sup>14</sup>A. H. MacDonald, Ph.D. thesis, University of Toronto

(1978), unpublished.

<sup>15</sup>K. L. Liu, A. H. MacDonald, J. M. Daams, S. H. Vosko, and D. D. Koelling, J. Mag. Magn. Mater. 12, 43 (1979).

<sup>16</sup>O. Jepsen and O. K. Andersen, Solid State Commun. 9, 1763 (1971).

<sup>17</sup>G. Lehmann and M. Taut, Phys. Status Solidi 54, 469 (1972).

<sup>18</sup>A. H. MacDonald, S. H. Vosko, and P. T. Coleridge, J. Phys. C 12, 2991 (1979).

<sup>19</sup>G. Gilat and N. R. Bharatiya, Phys. Rev. B 12, 3479 (1975).

<sup>20</sup>J. C. Shaw, J. B. Ketterson, and L. R. Windmiller, Phys. Rev. B 5, 3894 (1972).

<sup>21</sup>A true application of the Hellman-Feynman approach was employed which used the eigensolutions to take the bilinear product of an analytic derivative of  $(H-ES)$ . This is not the same as the scheme described by J. H. Wood [*Computational Methods in Band Theory*, edited P. Marcus, J. Janak, and A. R. Williams (Plenum, New York, 1971), p. 59]. In that scheme, the eigenvectors are not used and partial derivatives of the secular determinant are evaluated. That scheme avoids evaluating the eigenvectors at the price of evaluating  $4N$  determinants rather than 3 bilinear products.

<sup>22</sup>O. Gunnarsson, J. Phys. F 6, 587 (1976).

<sup>23</sup>S. H. Vosko and J. P. Perdew, Can. J. Phys. 53, 1385 (1975).

<sup>24</sup>G. Keiser and F. W. Wu, Phys. Rev. A 6, 2369 (1972).

<sup>25</sup>L. Wilk, A. H. MacDonald, and S. H. Vosko, Can. J. Phys. 57, 1065 (1979).

<sup>26</sup>B. N. Harmon, N. Elyashar, and D. D. Koelling, Bull. Am. Phys. Soc. 20, 364 (1975).

<sup>27</sup>F. Perrot, Phys. Status Solidi 46, 607 (1971); O. K. Andersen, unpublished; Phys. Rev. B 12, 3060 (1975).

<sup>28</sup>N. E. Christensen, J. Phys. F 8, L51 (1978).

<sup>29</sup>See, for example, F. Herman and S. Skillman, *Atomic Structure Calculations* (Prentice-Hall, Englewood Cliffs, New Jersey, 1963).

<sup>30</sup>F. J. Himpsel and D. E. Eastman, Phys. Rev. B 18, 5236 (1978).

- <sup>31</sup>K. A. Mills, R. F. Davis, S. D. Kevan, G. Thornton, and D. A. Shirley, *Phys. Rev. B* **22**, 581 (1980); G. Thornton, R. F. Davis, K. A. Mills, and D. A. Shirley, *Solid State Commun.* **34**, 87 (1980).
- <sup>32</sup>F. J. Himpsel, J. A. Knapp, and D. E. Eastman, *Phys. Rev. B* **19**, 2919 (1979).
- <sup>33</sup>R. J. Smith, G. J. Lapeyre, J. Anderson, and G. P. Williams, *International Conference on Transition Metals, Toronto, 1977* (Institute of Physics, London, 1978).
- <sup>34</sup>L. J. Sham and W. Kohn, *Phys. Rev.* **145**, 561 (1966).
- <sup>35</sup>D. H. Dye, S. A. Campbell, G. W. Crabtree, J. B. Ketterson, N. B. Sandesara, and J. J. Vuillemin, *Phys. Rev. B* **23**, 462 (1981).
- <sup>36</sup>For example, P. B. Allen, *Phys. Rev. Lett.* **37**, 1638 (1976).
- <sup>37</sup>J. W. Cable, E. O. Wollan, G. P. Felcher, T. O. Brun, and S. P. Hornfeldt, *Phys. Rev. Lett.* **34**, 278 (1975).
- <sup>38</sup>R. Maglic, T. O. Brun, G. P. Felcher, and Y. K. Chang, *J. Mag. Magn. Mater.* **9**, 318 (1978).
- <sup>39</sup>T. J. Watson-Yang, B. N. Harmon, and A. J. Freeman, *J. Mag. Magn. Mater.* **2**, 334 (1976).
- <sup>40</sup>T. J. Watson-Yang, A. J. Freeman, and D. D. Koelling, *J. Mag. Magn. Mater.* **5**, 277 (1977).
- <sup>41</sup>R. J. Weiss and A. J. Freeman, *J. Phys. Chem. Solids* **10**, 147 (1959).
- <sup>42</sup>P. K. Misra and L. Kleinman, *Phys. Rev. B* **5**, 4581 (1972).
- <sup>43</sup>See, for example, Y. Yafet, in *Solid State Physics*, edited by F. Seitz and D. Turnbull (Academic, New York, 1963), Vol. 14, p. 1.
- <sup>44</sup>O. K. Anderson and A. R. Mackintosh, *Solid State Commun.* **6**, 285 (1968).
- <sup>45</sup>J. F. Janak, A. R. Williams, and V. L. Moruzzi, *Phys. Rev. B* **11**, 1522 (1975).
- <sup>46</sup>D. H. Dye, J. B. Ketterson, and G. W. Crabtree, *J. Low Temp. Phys.* **30**, 813 (1978).
- <sup>47</sup>P. M. Raccach, R. N. Euwema, D. J. Stukel, and T. C. Collins, *Phys. Rev. B* **1**, 756 (1970).
- <sup>48</sup>S. H. Vosko, L. Wilk and M. Nasuir, *Can. J. Phys.* **58**, 1200 (1980).